IDEA League

Master of Science in Applied Geophysics

Research Thesis

Joint Surface-Downhole Microseismic Event Location

Dirk-Jan van Veen

August 10, 2016

Joint Surface-Downhole Microseismic Event Location

Master of Science Thesis

for the degree of Master of Science in Applied Geophysics at
Delft University of Technology
ETH Zürich
RWTH Aachen University
by

Dirk-Jan van Veen

August 10, 2016

Department of Geoscience & Engineering · Delft University of Technology
Department of Earth Sciences · ETH Zürich
Faculty of Georesources and Material Engineering · RWTH Aachen University

Delft University of Technology

Printed in The Netherlands, Switzerland, Germany

IDEA LEAGUE
JOINT MASTER'S IN APPLIED GEOPHYSICS

Delft University of Technology, The Netherlands
ETH Zürich, Switzerland
RWTH Aachen, Germany

Dated: *August 10, 2016*

Committee Members:

Prof. Dr. J. O. A. Robertsson (chair)

Dr. I. A. Vera Rodriguez

Dr. R. Ghose

Additional supervisor:

Dr. A. Gendrin

Abstract

A hydraulic stimulation operation in the Marcellus shale, Pennsylvania, was monitored by means of coalescence microseismic mapping, with receiver arrays downhole, in a horizontal well, and at the surface, in a radial geometry. The results of each survey are combined to obtain joint surface-downhole microseismic event location estimates that harvest the horizontal location constraint that results from surface monitoring, and the vertical location constraint that is expected from downhole monitoring. Downhole recordings were processed using two anisotropic velocity models with different axes of symmetry: one vertical (VTI) and one horizontal (HTI). Both velocity models are compared to determine which of the two is most suitable for a joint inversion. It was found that the HTI model removes an angle-dependent location uncertainty for calibration perforation shots that is present in the VTI model. However, the VTI model constrains the depth of the microseismic events better than the HTI model and is therefore the model that is used for the joint inversion. From the comparison it is suggested that an orthorhombic anisotropic velocity model could be requisite for more accurate location estimates. The joint inversion was performed by first matching surface- and downhole microseismic events in time (up to 40% success rate) and then in space (up to 97% success rate). Subsequently, the four-dimensional probability distribution functions (pdfs) that result from coalescence microseismic mapping of downhole data, are smoothed in horizontal direction to relax the horizontal location constraint, and then multiplied with the pdfs that result from surface monitoring. This yielded joint event locations that exhibit a horizontal position close to the one obtained from surface monitoring, and a vertical position close to the one obtained from downhole monitoring, a result that is considered an improvement with regards to the individual monitoring methods.

Acknowledgements

Above all, I thank Ismael Vera Rodriguez and Aline Gendrin for their continuous support, insightful discussions and meticulous reviews of my work, and whose door was always open whenever I had a question about my research or writing. It has been a great privilege to work with two such intelligent and caring people on a daily basis. I am thankful to Johan Robertsson for sustaining the connection with Schlumberger Gould Research, without which this thesis would not have existed. Thanks Johan, for responding quickly to my emails and for supporting the project from Zurich. I am also indebted to Phil Christie and Gwenola Michaud for their valuable reviews of my work. A special thanks goes out to Michael Williams, Takashi Mizuno and Shaoyong Su for their support regarding Microsoft Visual Studio. Lastly, I would like to express my gratitude to all of Schlumberger for providing the funds to conduct this research and especially to the people of Schlumberger Gould Research who provided an incredibly fun, stimulating and inspiring environment to work in.

Dirk-Jan van Veen
Cambridge,
August 10, 2016

Table of Contents

List of Figures

List of Tables

Nomenclature

Acronyms

CMM	Coalescence microseismic mapping
HTI	Horizontal transversely isotropic
LUT	Look-up-table
pdf	Probability density function
SNR	Signal-to-noise-ratio
STA/LTA	Short-term-average windown length over long-term-average window length
RMS	Root mean square
VTI	Vertical transversely isotropic

Terminology

P	Pressure [wave]
Sh	Horizontal shear [wave]
Sv	Vertical shear [wave]
CMM cube	Four-dimensional map that represents the pdfs of event location and origin time; the result of summation of the probability density functions at each nodepoint in the LUT and subsequent interpolation between the nodes.
CMM shape	Dominant shape of the pdf in the CMM cube
event location	Maximum likelihood location, usually at the center of the CMM shape
joint	Involving information from both downhole and surface monitoring

Variables and Parameters

M_0	Seismic moment
c	Velocity
Ω_0	Level of low frequency spectrum
R	Hypocentral distance

M_w	Magnitude
a	Constant called 'productivity'
W_L	Long time window
W_S	Short time window
α	Slope of linear function relating the variance of the detection function and pick uncertainty
d	Distance
L_{R_i}	Logarithm of combined onset and forward modelling pdf
t_0	Seismic event origin time
T_{obs}	Observed travel time
T_{mod}	Modelled travel time
l^{pred}	Predicted location of microseismic event
l^{true}	True location of microseismic event
T_{il}	Observed onset time
τ_{il}	Computed onset time
Θ_{il}	Observed polarisation angle
θ_{il}	Computed polarisation angle
σ_{Tl}	Standard deviation of observed onset time
$\sigma_{\theta l}$	Standard deviation of observed polarisation angle
α_0	S-wave velocity
β	P-wave velocity
θ	Angle of incidence
t	[travel] time
$\bar{s}$	Vector containing spatial position of a microseismic event
t_{g_i}	Forward modelled travel time
ϵ, δ, γ	Thomsen's parameters
$\Delta x, \Delta y, \Delta z$	Grid cell dimensions
V_{min}	Slowest velocity
σ_R^2	Variance of a Gaussian that fits the onset of a signal
σ_D^2	Variance of a Gaussian that fits the maximum of the detection function
σ_G^2	Variance of a Gaussian that represents the uncertainty of forward modelling (travel time prediction)
t_{D_i}	Maxima of the detection function

Other

$^\circ$, [deg]	Degrees

Chapter 1

Introduction

1-1 Passive Seismic Monitoring and Hydraulic Fracturing

Shale oil and gas have made a solid and permanent entry into the global energy supply in the last decade. US shale oil output has grown from 111,000 bpd in 2004 to 4.86 million bpd in April 2016 (U.S. Energy Information Administration, 2016; PwC, 2013). According to the BP Energy Outlook (2016), shale gas will account for 24% of the global gas production by 2035. Because the global energy demand is expected to outpace the increase in renewable energy output, hydrocarbons are expected to still account for 60% of the global energy growth from 2014 to 2035 make up almost 80% of global energy supply until 2035 (figure 1-1).

Shale reservoirs typically exhibit low permeability and therefore need artificial creation of flow paths, which is achieved by hydraulic fracture stimulation. This process entails first perforating the well in the zone of interest, and then, pumping a mixture of water, proppant and chemical additives into the formation at high pressure, such that the rock breaks. After the fracking fluid has flown into the cracks, the proppant prevents the fractures from closing once the pressure is released. Hydrocarbons can then flow to the well through the newly created open cracks.

Microseismic monitoring is often used in the oil and gas industry to understand the response of the reservoir to stimulation or fluid injection. This improved understanding helps oil and gas operators to better manage the injection process to optimize reservoir stimulation or production. Real time monitoring and processing of microseismic data also allows reduction of environmental hazards, because the stimulation process can be stopped when rocks are breaking in undesirable areas, such as near water aquifers or preexisting faults (Maxwell et al., 2010; Duncan and Eisner, 2010b). Hence an accurate processing sequence of passive seismic data is indispensable for obtaining the right event locations to make the right decisions in the field.

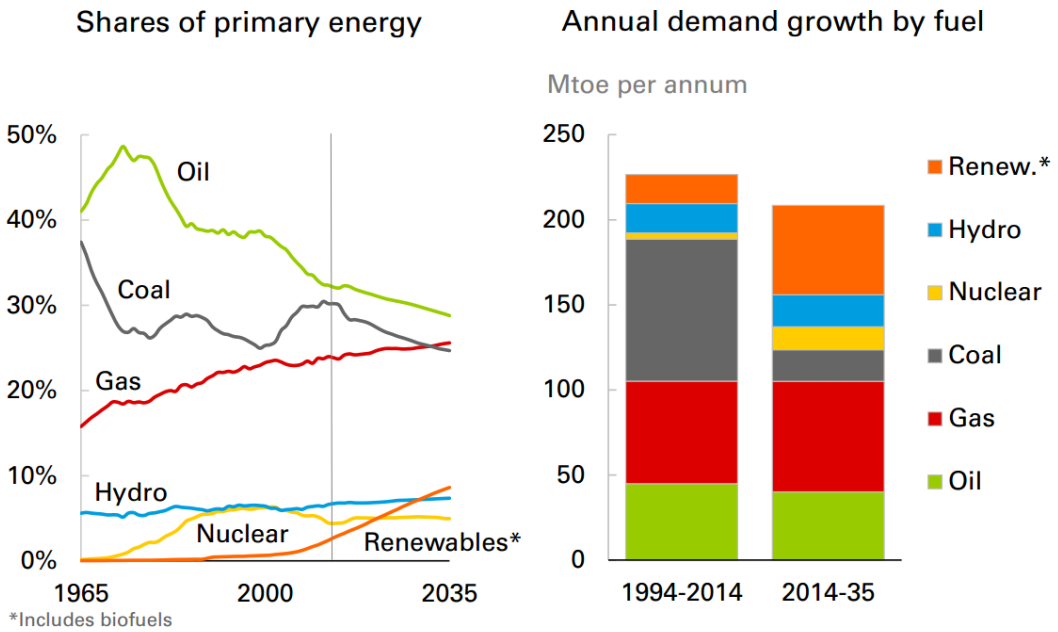

Figure 1-1: Left: Renewables, gas and hydro will make up a larger part of the global energy mix. Oil remains the primary source of energy. Right: renewables will account for the greatest growth in energy demand. (BP, 2016)

1-2 Nature of Microseismic Events

A seismic event is the result of rock failure, which results in concurrent generation of P- and S-waves (Aki and Richards, 1980). In the context of the oil industry, microseismicity can be due to hydraulic fracturing, fluid injection or fluid extraction. More often, the purpose of microseismic event location in hydraulic fracturing is to estimate the stimulated reservoir volume, infer the geometry of hydraulic fractures or evaluate fracture height growth and the rock type (Maxwell et al., 2010; Duncan and Eisner, 2010b). The type of rock failure can be determined by looking at the source mechanism of a microseismic event (Aki and Richards, 1980). The source mechanism also determines the polarity of the recorded signal. Microseismic events are associated with the creation of new fracture planes or with the interaction of the injection treatment with pre-existing fractures. Several authors propose shear slip as the dominant origin of microseismic events induced by hydraulic fracturing (Warpinski et al., 2004; Maxwell, 2011)(figure 1-2). Elevated pore pressure reduces stress along pre-existing fractures and thereby induces shear slip (Pearson, 1981). Evans et al. (1999) argue that since shear slip can be triggered by small pore-pressure increases, it can be expected that microseismic events also take place in the rock beyond opened hydraulic fractures. This means that maximum hydraulic fracture lengths and widths do not strictly constrain the area in which microseismic events can take place (Rutledge and Phillips, 2003).

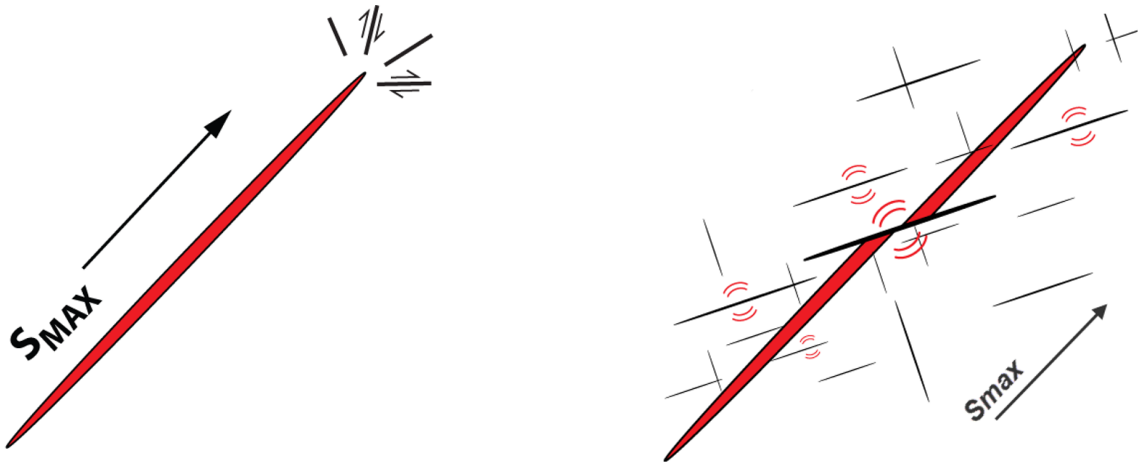

(a) Stress around a hydraulic fracture in a homogeneous environment

(b) Stress around hydraulic fracture in naturally fractured environment

Figure 1-2: Stressfields in homogeneous and naturally fractured environments. Modified from Schlumberger internal document.

1-3 Aim of the Project

Microseismic events are currently monitored by placing sensors either at surface or downhole (Peyret et al., 2012). Surface microseismic surveys yield robust horizontal event locations but suffer from larger uncertainties in depth (Grechka, 2015; Eisner et al., 2009; Anikiev et al., 2014). Downhole seismic arrays on the other hand, provide better constraint on the distance of the event from the monitoring array, but present significant azimuthal location uncertainty, especially for events far away from the monitoring well (Grechka and Yaskevich, 2013). In this study, we attempt to combine the two types of measurements in a joint inversion, in order to achieve more accurate localisations as a result of tighter combined constraints.

Microseismic event location is a complex problem, as event locations, origin times, and velocity model derivations are effectively interdependent. One way to approach this problem is to calculate a velocity model using perforation shots, whose location is assumed to be known (Bradford et al., 2013; Probert et al., 2013). Another way to approach the problem is to simultaneously invert for all unknown parameters (Zhang and Thurber, 2003; Grechka, 2015; Blias and Grechka, 2013), which results in joint microseismic event locations and velocity model derivation.

Here, I rely on the velocity model retrieved by Becker (2015), for both surface and downhole surveys. Since Becker (2015) identified an azimuthally dependent mismatch between modelled and observed travel times in the case of the downhole survey, we first attempt to improve our downhole velocity model by considering HTI (Horizontal Transversely Isotropic) anisotropy instead of VTI (Vertical Transversely Isotropic) anisotropy. HTI anisotropy is indeed expected in media with aligned vertical fractures. For events identified from both surface and downhole surveys, the Coalescence Microseismic Mapping (CMM) (Drew et al., 2013) objective functions (discussed in the next chapter) are analysed and different possible combinations are investigated to produce a joint solution.

1-4 Dataset

The Marcellus shale is a black-shale unit of Middle Devonian age that stretches across the Appalachian basin and underlies the states of Pennsylvania, Ohio, New York and West Virginia in the northeastern United States (Neuhaus et al., 2012) (figure 1-3). The US Geological Survey estimates that the Marcellus shale may hold up to 2.4×10^{12} m^3 of natural gas (Coleman Jr et al., 2011). Because of this potential, the Gas Technology Institute, with funding from the Research Partnership to Secure Energy for America (RPSEA), has set up an industry research cooperation with Range Resources and Schlumberger to identify and overcome technical and environmental challenges that could impede gas production from unconventional reservoirs and the Marcellus shale in particular. The microseismic dataset studied in this thesis was acquired as part of this cooperation.

The survey was conducted in January and February of 2011 on a well site in Washington County, Pennsylvania, 40 km South-West of Pittsburgh. Seven Horizontal wells were drilled from a multi-well pad, targeting the upper Marcellus shale at approximately 2000 meters below the surface or 1650 meters below mean sea level. Although the lower Marcellus shale is considered to be a better quality reservoir, the upper part was targeted in this research project because past trials have shown that the upper part lends itself better to hydraulic stimulation (Ciezobka, 2012).

The wells branch out in a northwest direction, perpendicular to the maximum horizontal stress. The horizontal wellbores were drilled in a parallel fashion with a lateral distance of about 150 meters and range from 900 to 1325 meters in length (figure 1-4). Over the course of the project, which lasted 27 days, hydraulic fracture treatment was performed in 94 stages. Prior to each fracking stage, three perforation shots were fired at intervals of 30 m along the horizontal part of the wellbore. Subsequently, proppant was pumped and a plug set before moving to the next stage.

Seismic wavefields were monitored concurrently at the surface and downhole during perforation and fracking. For downhole monitoring, a Schlumberger Versatile Seismic Imager was used. It consisted of eight 3-component geophones, spaced 30 m from one another in the horizontal section of the monitoring well (2H, see figure 1-4)). Geophones were recording with 0.5 ms sampling rate. To ensure close proximity to the stimulated section of the reservoir, the tool was moved four times within the monitoring well. The 284 hours of downhole recordings available for this project include 62 out of 94 fracturing stages. Surface acquisition was made using 1082, 1-component 'Geospace Seismic Recorder' geophones laid out in 10 branches in a radial fashion. The geometry of the lines was dictated by environmental constraints (figure 1-4). An average receiver separation of 25 meter and a sampling rate of 2 ms was maintained. In total, 435 hours of surface recordings were acquired which included all 94 fracking stages.

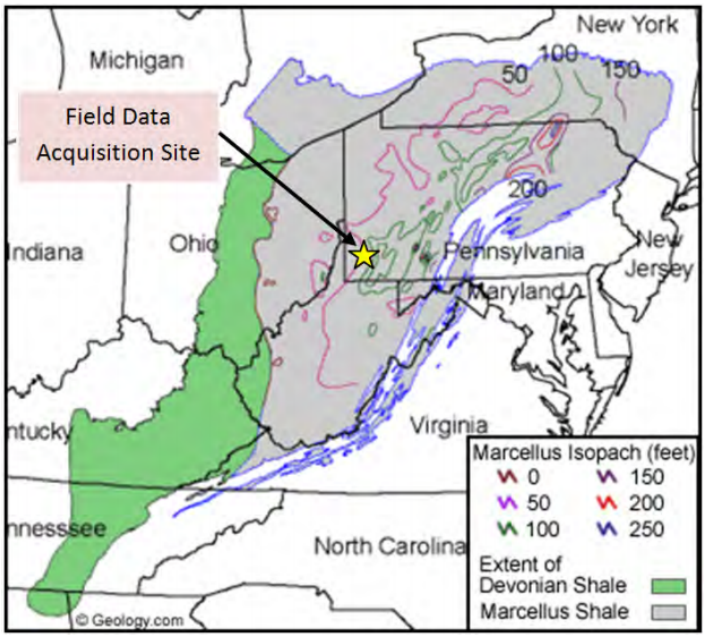

Figure 1-3: Location of the survey is denoted with yellow star. Ciezobka (2012)

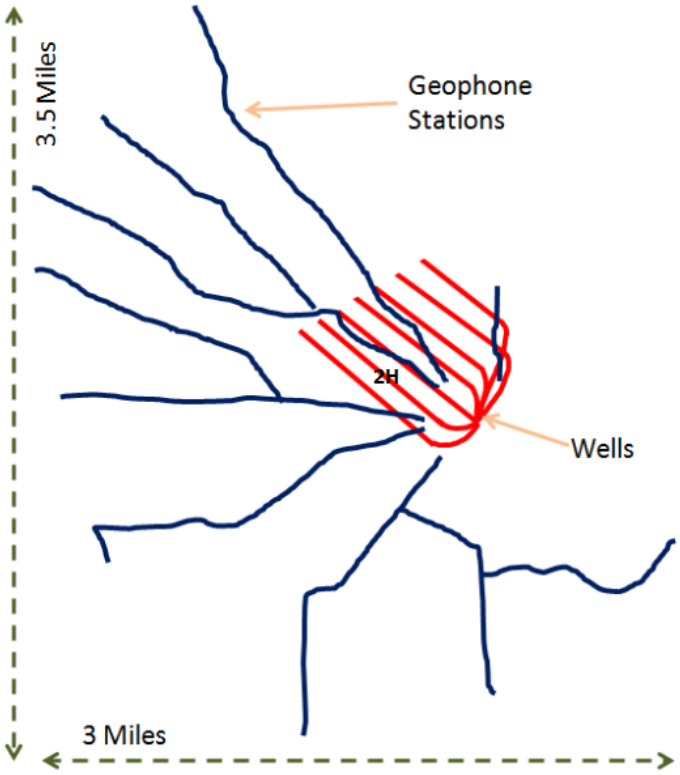

Figure 1-4: Geometry of the horizontal wells is depicted in red. The geometry of the surface array in blue. Ciezobka (2012)

Chapter 2

Theoretical Context

This chapter provides a brief background on the rock mechanics behind induced microseismicity, the basic equations that govern inversion in a geophysical context, and an introduction to the microseismic mapping method that is used in this thesis.

2-1 Mechanics of Induced Seismicity

For industrial hydraulic fracturing, horizontal wells are drilled parallel to the minimum stress direction so that large fractures can form in planes perpendicular to the horizontal well. Due to the weight of the overburden, the minimum stress direction in most basins is horizontal, resulting in long vertical hydraulic fractures (Anderson, 1905; Hubbert and Willis, 1957). Hydraulic fractures are often confined to a single formation because layering produces strength boundaries that inhibit vertical growth (Economides et al., 2000). Microseismic events are often associated with reactivation of natural fractures around a tensile hydraulic fracture. Since pre-existing fractures are likely to fail in shear before they fail in tension (Rutledge et al., 2004), they form in directions away from the maximum horizontal stress direction. When the injection fluid is pumped downhole, the pore pressure is increased, which thereby reduces normal stress. As a result, Mohr's circle is shifted leftward, which promotes shear failure (figure 2-1) (Scholz, 2002).

Shear failure events can be characterized by the source spectra of the induced seismic events: low frequency amplitude of the spectrum and corner frequency (Brune, 1970). These parameters are used to estimate seismic moment and magnitude distribution, with which microseismic events can be distinguished from tectonic events (e.g. De La Pena et al., 2011). Seismic moment M_0 is defined as:

$$M_0 = \frac{4\pi c^3 R \Omega_0}{A} \quad , \tag{2-1}$$

where c is velocity (the compressional and shear velocities are selected for the P- and S-waves, respectively), ρ is the density, R is the hypocentral distance, Ω_0 the level of the low frequency

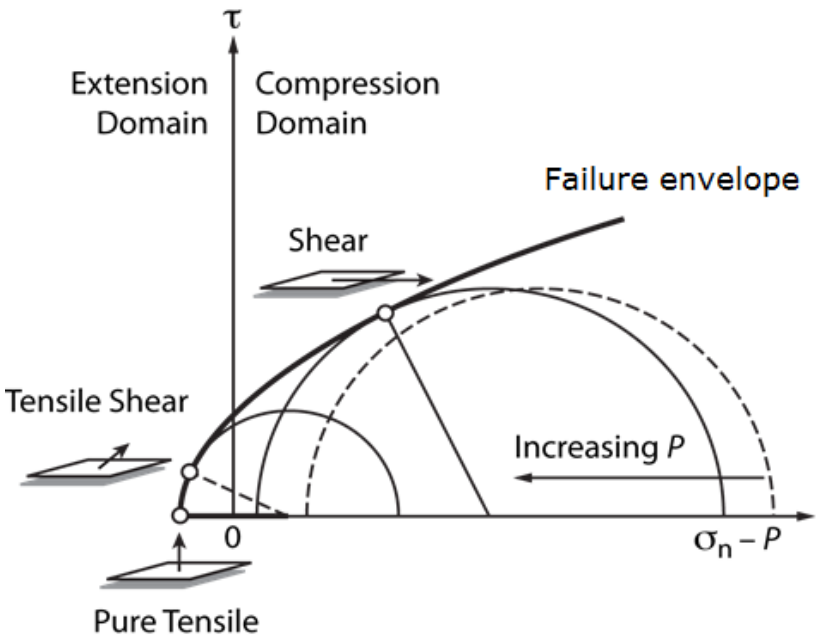

Figure 2-1: Mohr-diagram relating the failure envelope to the different types of rock failure. The horizontal axis depicts normal stress, the vertical axis shear stress. Mohr's circle shifts to the left when the pore pressure P is increased. Modified from Schlumberger internal document.

spectrum, and A is the average radiation coefficient ($A = 0.52$ and 0.63 are used for the P- and S-waves, respectively)(Aki and Richards, 1980). The magnitude of an earthquake M_w is related to seismic moment following

$$M_w = \frac{2}{3} log M_0 - 6.0 \tag{2-2}$$

(Kanamori, 1977), where M_0 is in units of N m. The Gutenberg-Richter relationship (Gutenberg and Richter, 1956) establishes the dependence between the number of seimic events and their magnitude:

$$log(N) = a - bM_w \quad , \tag{2-3}$$

where N is the number of events having a magnitude larger than M_w, a is a constant called productivity and b is a constant called *b-value*. For tectonic seismic events, b is typically close to 1.0 (Bender, 1983). For microseismic events induced by hydraulic fracturing, b-values are larger. b-values of 2 and higher have been reported by De La Pena et al. (2011). Williams and Calvez (2013) on the other hand, cap b-values at a theoretical maximum of 1.5. In a practical sense this logarithmic relationship means that, in a microseismic dataset, if 1 microseismic event of magnitude X is observed, we will likely observe ∼10 microseismic events of magnitude X-1, and ∼100 microseismic events of magnitude X-2.

2-2 Coalescence Microseismic Mapping

Coalescence Microseismic Mapping (CMM) is a method developed by Drew et al. (2013) to locate microseismic events. CMM forms a hybrid between linearised inversion of discrete arrival time picks and direct imaging methods. Linearised inversion has a relatively straightforward procedure. However, unidentified mis-picks and outliers can introduce bias to the localisation of a seismic event. Direct imaging, where data are backpropagated to a focus at the source location and origin time, allows for more accurate positioning in complex geological settings, and is capable of incorporating tilted transverse isotropy, but requires an accurate velocity model and a densely sampled wave field (Baysal et al., 1983; Whitmore et al., 1983). The method combines the strengths and avoids the weaknesses of both techniques by using a Bayesian formulation of event location traveltime inversion. The CMM algorithm uses three main steps.

1. A 3D-grid that covers all potential source locations in the subsurface is created, which we will refer to as a look-up-table (LUT). Traveltimes from each node in the LUT to each receiver are calculated with a given velocity model.
2. The Short Term Average/Long Term Average ratio (STA/LTA) is calculated for each seismic trace. Ratios above a specified threshold are marked as a potential microseismic event. A Gaussian is fitted to the STA/LTA function corresponding to each potential P, Sh and Sv arrival and, as argued by Drew et al. (2013), the Gaussian may be assumed to approximate the probability density function (pdf) of the signal onset. The obtained probability density function (pdf) is a representation of the signal onset. Indeed, a higher value of this curve means a higher likelihood of a microseismic event.
3. The Gaussian pdf of the signal onset function is migrated back through the 3D grid by performing an exhaustive search over the pre-computed traveltimes in the grid at each node to see which nodes are probable event locations (figure 2-2). Summation of the probability density functions at each nodepoint and interpolation between the nodes yields a four-dimensional map that represents the pdfs of event location and origin time for each microseismic event. Throughout this thesis these collections of pdfs at different times will be referred to as a CMM cube.

The STA/LTA ratio can be expressed as an arrival onset function $f_D(t)$ for the amplitude of a seismic signal $y(t)$ over a short time window length W_S and a long time window length W_L:

$$f_D = \frac{W_L \int_0^{W_L} |y(t+\tau)|\, d\tau}{W_S \int_0^{W_S} |y(t+\tau)|\, d\tau} \tag{2-4}$$

(Drew et al., 2013). STA/LTA onset functions are calculated separately for P- Sh- and Sv-waves in each recording, in order to obtain the signal onset for each wavefield component such that seismic attributes can be calculated. Figure 2-3 demonstrates the use of an arrival onset function for a few seismic traces recorded near the Askja volcano in Iceland. The function works correctly for the vast majority of traces, however for trace DYNG in the S-wave recordings of figure 2-3, the onset is calculated to be too early. In such cases, the phase

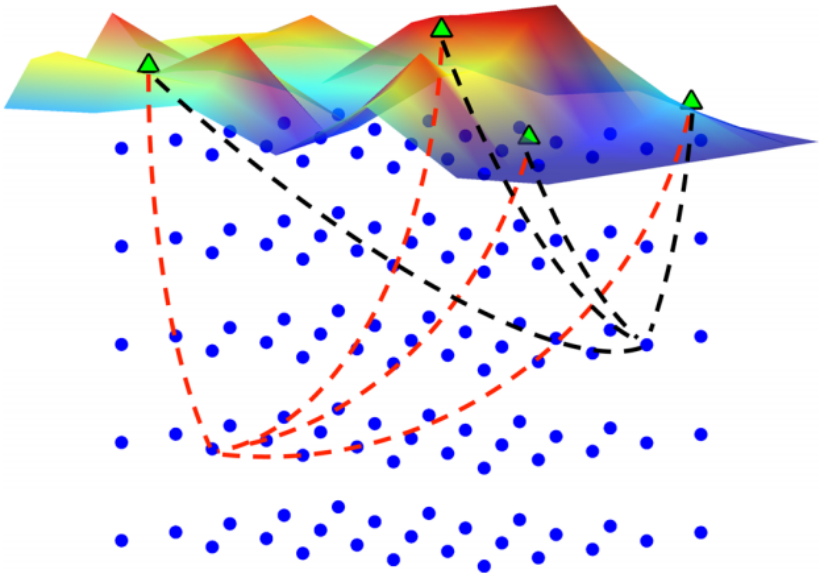

Figure 2-2: Schematic setup of a seismic experiment. Blue dots represent the nodes of the 3D grid, green triangles on the surface denote receivers. The onset pdf's are back-migrated at each time-step using the velocity model and the 3D-grid. The onset functions at each nodepoint are summed. Adopted from Drew et al. (2013).

arrival will be migrated away from the true coalescene point by the wrong LUT (S-wave LUT applied to P-wave onset signal or vice versa) so that neither the corresponding P-wave nor S-wave contributes to the coalescence, or biases the solution (Drew et al., 2013).

The STA/LTA detection treshold is commonly set at a SNR between 2 and 3. In such cases, a Gaussian is fitted to the arrival onset (figure 2-4). The larger the amplitude of the arrival's waveform, the narrower the Gaussian that can be fitted to the arrival's waveform. Consequently, the choice of detection threshold effectively equals appointing a maximum picking error (Drew et al., 2013).

The CMM algorithm makes use of two key uncertainty distributions that determine the coalescence function:

1. The 'onset pdf', representing the likelihood and uncertainty of traveltime picks, which is constructed from the STA/LTA onset function.
2. The 'forward modelling pdf' that represents the uncertainty in traveltime prediction, which is due to uncertainty in the velocity model and hence fluctuates for different nodes in the LUT.

For the sake of brevity, we skip the full derivation of the CMM algorithm from these two functions (see Drew et al. (2013) for the full mathematical justification) and jump right to the final form of the coalescence function as it is implemented in this thesis:

$$f_C(t, \bar{s}) = exp\left\{\alpha \sum_{i=1}^{n} L_{R_i}(t_0 + t_{g_i}(\bar{s}))\right\} \quad , \tag{2-5}$$

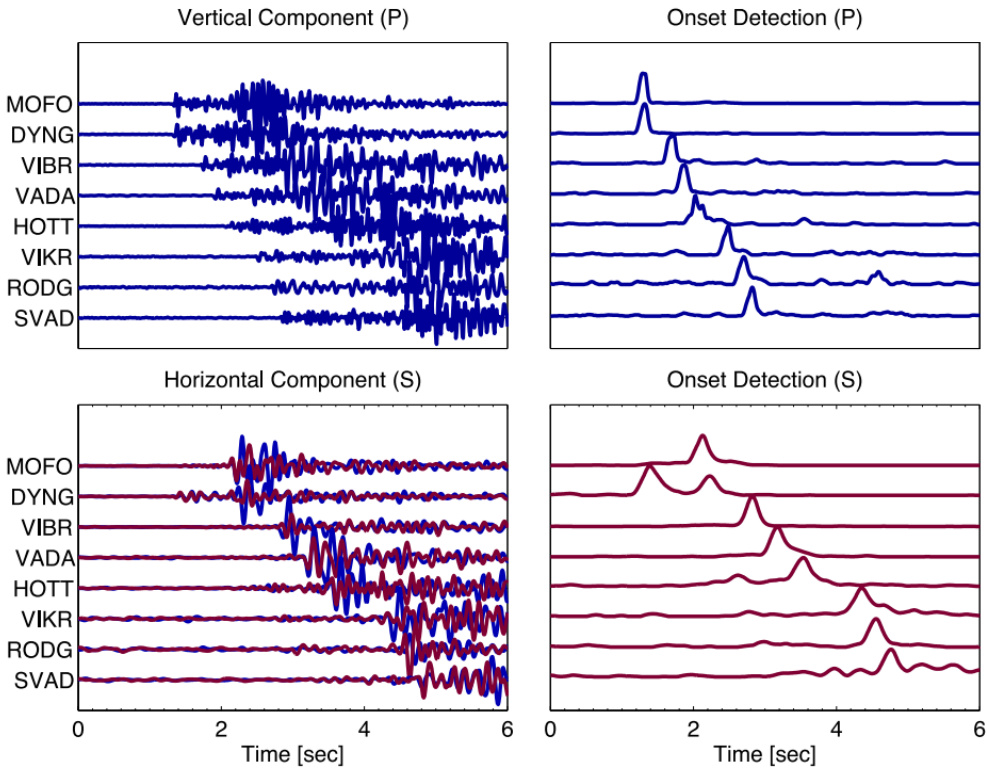

Figure 2-3: P- (top) and combined S-wave (bottom) recordings from a shallow microseismic event near Askja, Iceland, and their corresponding arrival onset functions (S-wave is computed from rms summation at each time step of both Sv and Sh signals). Most signal onsets are calculated appropriately, but for S-wave DYNG recording, the signal onset it calculated to be too early. Incorrect phase arrivals like these will be migrated away from the true coalescence point by the wrong look-up table. Adopted from Drew et al. (2013)

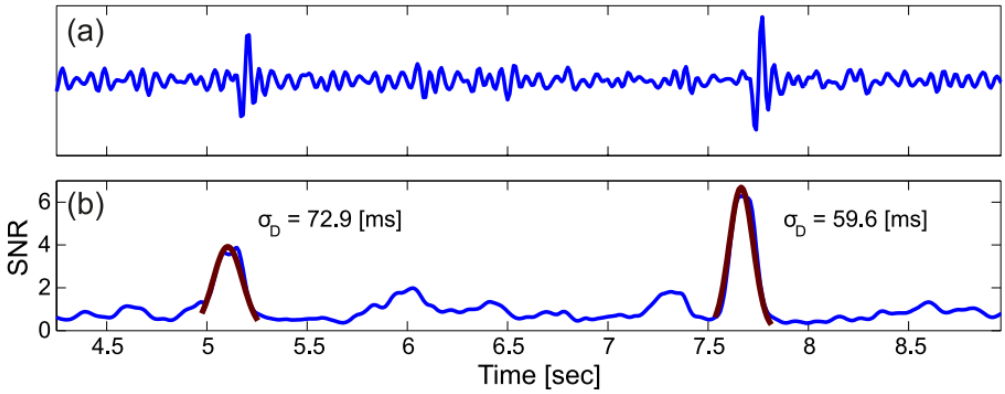

Figure 2-4: Gaussian fitting to arrival onsets. (a) Synthetic arrivals with recorded noise superimposed. (b) Signal onset function (STA/LTA) with red Gaussian curves fitted to arrivals. Uncertainties are listed next to Gaussians. Adopted from Drew et al. (2013).

where α is the slope of a linear function relating variance of detection function and pick uncertainty, L_{R_i} is the logarithm of the combined onset and forward modeling pdf, t_0 is the microseismic event's origin time and $t_{g_i}(\bar{s})$ the forward modelled traveltime for hypocenter at $\bar{s}$. Note that for numerical applications the time component of the four-dimensional coalescence function has to be broken up into a discrete time window with corresponding CMM cubes for each timestep.

Chapter 3

Event Location from Downhole Data

The location accuracy of microseismic events is dependent on the accuracy and robustness of the velocity model (Warpinski, 2009). Becker (2015) processed the dataset considered in this thesis with a VTI (vertical transverse isotropy) velocity model. This velocity model was calibrated with the perforations from multiple hydraulic fracturing stages so as to be robust enough to use for processing on as many hydraulic fracturing stages as possible, for both surface and downhole data. Other authors choose to calibrate a velocity model for each stage, because they consider that velocity variations in the stimulated field are important to take into account (Bardainne and Gaucher, 2010). A choice between these two approaches depends on the field and on the geology. Whenever one single velocity model provides accurate perforation shot locations throughout a field, with robust well calibration, it will contribute to precise location estimates. The event locations of the calibration shots that Becker (2015) found with the VTI velocity model, were subject to an uncertainty bias: event locations close to the receiver string showed greater uncertainty than the ones far away from the receiver string. Fracture events also displayed a systematic bias that appeared to correlate with the azimuthal ray angle. In this chapter, I investigate the effect of a horizontal transversely isotropic (HTI) velocity model on the event location and bias in event location uncertainty, and compare the HTI results to the VTI results.

3-1 Velocity Model Construction

Becker (2015)'s initial VTI velocity model was based on vertical compressional velocity, vertical shear velocity and density logs that were obtained from the study site over an interval ranging from 1370 m to 1611 m depth TVDSS (true vertical depth sub-sea). The model was simplified by applying Backus-averaging (Backus, 1962), which yielded seven layers with constant VTI properties. The velocity model as a whole was then shifted down 40 m to place the target layer at its correct depth and tilted 1 degree towards the north-east to account for the subtle dip of the reservoir (Becker, 2015). During the calibration of the VTI model, Becker (2015) reported a systematic bias in traveltime residuals associated with the horizontal angle

of wave arrival. This systematic bias reflects horizontal variations of velocity, which cannot be accounted for with a VTI model. Therefore, this thesis investigates whether this bias can be removed with the use of an HTI model, and how that impacts microseismic event locations. The HTI velocity model is similar to the VTI model, with the exception that the axis of symmetry for the velocity variation is horizontal. Notice that the anisotropy of the medium could be more complex than that of an HTI model, but since the treatment wells and the downhole array of receivers are roughly at the same depth, the ray paths between sources and receivers are expected to be nearly horizontal and constrained to the target layer. Therefore, the available data is ideal to constrain an HTI model, which, in this case, was also simplified to a homogeneous layer. The axis of symmetry for the model was selected parallel to the orientation of the wells. This choice sets the axis of symmetry in the direction of minimum principal stress, and was made for convenience. An incorrect selection of the axis of symmetry can render the HTI model inappropriate, resulting also in anisotropy parameters with little physical meaning. In this thesis, the work is limited to finding a set of parameters that fits the observations in the range of angles of interest. No attempt is made to ascribe a physical meaning to them.

3-2 Calibration

For the calibration of the velocity model, the perforation shots need to be first detected in the downhole recordings, which was achieved by computing the short-time-average over long-time average (STA/LTA) ratio of each trace (Wong et al., 2009). If a recording exhibited an STA/LTA ratio larger than 2 on at least 50% of the traces, an event was triggered. From the pool of triggered events, manual selection of perforation shots was carried out based on a match with the shot times listed in the observer notes and the shape of the waveforms. Selected waveforms displayed clear and consistent P-wave arrivals combined with weaker shear wave arrivals, consistent with an approximately isotropic, volume injection source, in contrast to shear failure of a microseismic event. Once the shot locations had been assigned to the identified perforations, P-, Sh- and Sv-arrivals were picked manually. Close attention was paid to picking phase-consistent and first breaks only (figure 3-1). Dubious or uncertain arrivals were not used. About 95 percent of P-waves were successfully picked with an estimated error of 1 ms, Sh and Sv arrivals were significantly less obvious to spot with only 20 percent of them picked for calibration purposes. This process was repeated for 4 different tool string positions. The HTI velocity model was then calibrated using 80 detected perforations from wells 3H, 4H, 10H and 11H and geophone string positions 1, 2 and 3, in contrast to the 21 perforations from the same wells and only string position 1 in Becker (2015)'s VTI model (tables 3-2 and 3-3). Traveltimes from perforation shots in well 9H were discarded because this well is shallower than the other wells. The geology changes in the vertical direction and well 9H is positioned in a layer with different velocity properties, violating the homogeneous assumption made for the HTI model.

Thomsen's weak anisotropy parameters ϵ, δ and γ were selected to describe the HTI model. The parameters were obtained by applying a non-linear inversion technique (Mizuno et al., 2010) that minimises the misfit between traveltimes predicted by the velocity model and observed traveltimes by iteratively adjusting the anisotropy parameters. P-wave traveltime t_P, horizontal S-wave traveltime t_{Sh}, and vertical S-wave traveltime t_{Sv} are computed by

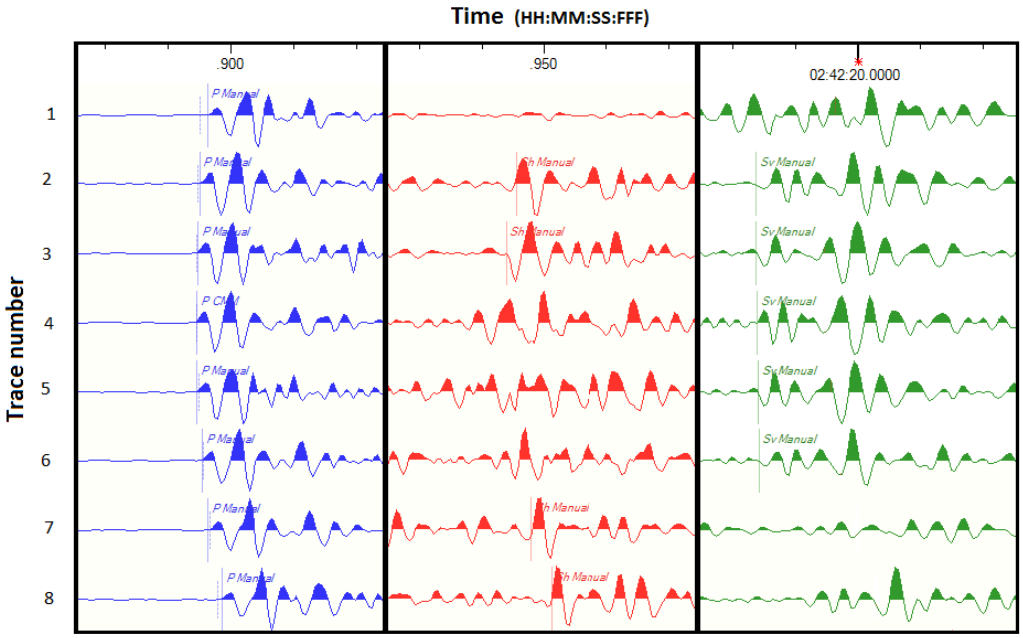

Figure 3-1: Traveltime picks for the 3rd perforation in well 3H during fracking stage 2. P-, Sh-, and Sv-waves are denoted in blue, red and green respectively. A 3-300 Hz Butterworth bandpass filter is applied to the traces; amplitudes are normalised by trace. The figure displays real chronological order of arrivals (see timescale).

equations 3-1, 3-2 and 3-3 modified after Thomsen (1986):

$$t_P(\theta) = \frac{d}{\alpha_0}[1 + \delta sin^2(\theta)cos^2(\theta) + \epsilon sin^4(\theta)]^{-1}, \tag{3-1}$$

$$t_{Sh}(\theta) = \frac{d}{\beta_0}[1 + \gamma sin^2(\theta)]^{-1}, \tag{3-2}$$

$$t_{Sv}(\theta) = \frac{d}{\beta_0}[1 + \frac{\alpha_0^2}{\beta_0^2}(\epsilon - \delta)sin^2(\theta)cos^2(\theta)]^{-1}, \tag{3-3}$$

where α_0 and β_0 are the speeds of P- and S-waves, respectively, along the axis of symmetry. Variable d is the source-receiver distance, and θ the angle between the wavefront normal and the axis of symmetry in the transverse isotropic medium, assumed to approximate the ray angle between source and receiver. The HTI model was calibrated in two different ways. In the first scenario, the calibration algorithm solved for the Thomsen's parameters and the compressional and shear velocities along the horizontal axis of symmetry. In this case, only the Vp/Vs ratio was fixed, where the initial values of velocity corresponded to those of the VTI model. In the second scenario, the values of Vp and Vs along the axis of symmetry are consistent with the VTI model. Therefore, only the Thomsen's parameters were estimated. Table 3-1 shows a comparison between calibrated VTI and HTI velocity model parameters in the two scenarios described.

Table 3-1: Differences between calibrated VTI and HTI velocity model parameters. The VTI values correspond only to the target layer. See text for description of HTI scenarios 1 and 2. While negative delta is physically possible for VTI media formed from shales (Miller and Singh, 1994; Sayers, 2005) the parameters found here require more than a stress field to explain. However, the HTI model does indeed fit the data better than the VTI model.

	$V_p(m/s)$	$V_s(m/s)$	$\rho(kg/m^3)$	ϵ	δ	γ
VTI	3252	1786	2.09	0.01	N/A	0.30
HTI scenario 1	5260	2277	2.09	0.00	-0.11	0.44
HTI scenario 2	3282	1786	2.09	0.00	0.06	0.29

The traveltime residuals in model HTI scenario 1 improve compared to the residuals from the VTI model (tables 3-2 and 3-3). Traveltime residuals from HTI scenario 2 do not evidently improve compared to the VTI model. A common element in all the calibrated models is a large γ value, reflecting a significant variation in the speed of propagation of Sh waves. ϵ converges towards zero in the two scenarios tested for the HTI model with δ displaying significantly different values. In the case of the VTI model, δ was not constrained by the travel paths between perforation shots and receivers. Considering that HTI scenario 1 provides a better explanation of the observations, it was chosen to estimate location results to compare against the VTI model. Figure 3-2 displays the velocity profiles of the VTI and the HTI scenario 1 velocity models.

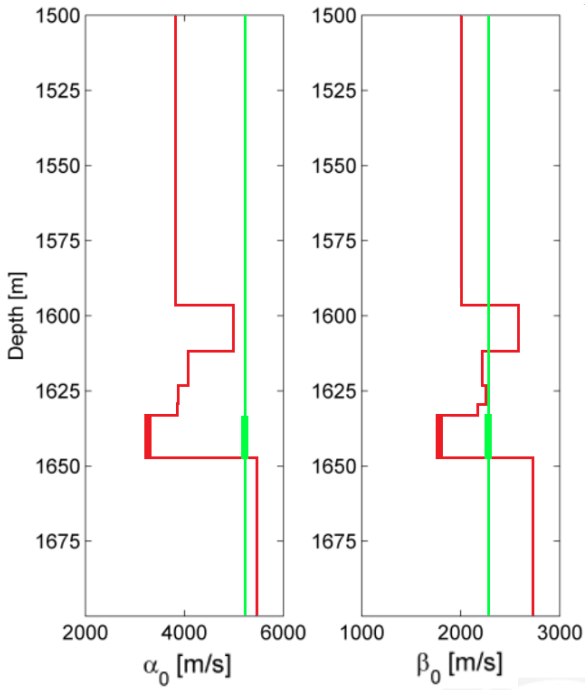

Figure 3-2: Velocity profiles for the VTI (red) and HTI scenario 1 (green) velocity models. The boldface interval signifies the target layer.

Table 3-2: Traveltime residuals for P- Sh- and Sv-arrivals for the calibration of HTI scenario 1 and 2. Each table entry represents the mean travel time residual over several perforation shots for that particular receiver, calculated by taking the difference between observed and modelled traveltimes $T_{obs} - T_{mod}$.

(a) HTI scenario 1 calibration residuals

(b) HTI scenario 2 calibration residuals

Receiver	Δt_P [ms]	Δt_{Sh} [ms]	Δt_{Sv} [ms]	Δt_P [ms]	Δt_{Sh} [ms]	Δt_{Sv} [ms]
pos. 1 rec. 1	0	0.2	0.8	0.5	1.1	1.5
pos. 1 rec. 2	-0.1	1.2	0.2	0.4	1.3	-1.2
pos. 1 rec. 3	-0.1	-0.2	0.6	0.4	0.0	0.0
pos. 1 rec. 4	0	-0.6	1.4	0.1	-1.1	3.2
pos. 1 rec. 5	0	-1.5	0.6	0.1	-2.0	4.1
pos. 1 rec. 6	0.4	0.5	0.9	-0.2	-0.5	4.5
pos. 1 rec. 7	0.2	1.6	0.7	-0.6	0.8	0.9
pos. 1 rec. 8	0.4	-0.1	-1.5	-1.4	-1.7	0.5
pos. 1 RMS	0.2	0.9	0.9	0.6	1.2	2.6
pos. 2 rec. 1	0	0.5	-0.6	-0.6	1.2	-2.5
pos. 2 rec. 2	-0.2	0.4	-1.4	-0.5	1.1	0.2
pos. 2 rec. 3	-0.2	0	-0.5	-0.1	0.6	1.5
pos. 2 rec. 4	0.1	0.2	0.7	0.4	0.4	2.2
pos. 2 rec. 5	0	1.4	0.5	0.5	1.6	0.5
pos. 2 rec. 6	0	0.9	2.1	0.5	0.7	-5.8
pos. 2 rec. 7	0	-0.8		0.5	-1.5	
pos. 2 rec. 8	0	-1.6		0.3	-3.1	
pos. 2 RMS	0.1	0.9	1.1	0.5	1.5	2.8
pos. 3 rec. 1	-0.3	0.8	-0.1	-1.4	1.2	0.1
pos. 3 rec. 2	-0.6	0.2	0.2	-0.6	0.8	2.5
pos. 3 rec. 3	-0.4	-1	1.2	-0.6	-1.2	-0.2
pos. 3 rec. 4	0	0.9	0.5	0.1	0.5	0.6
pos. 3 rec. 5	0.3	0.9	-0.3	0.8	0.2	1.6
pos. 3 rec. 6	0.6	-1.5	-1.3	0.8	-2.8	2.2
pos. 3 rec. 7	0	0.6		1.6	-1.6	
pos. 3 rec. 8	0.2	-2.3	0.5	1.1	-5.5	2.2
pos. 3 RMS	0.4	1.2	0.7	1.0	2.4	1.6
total RMS	0.3	1.0	0.9	0.7	1.8	2.4

Table 3-3: Traveltime residuals for P- Sh- and Sv-arrivals for the calibration of the VTI velocity model. Each table entry represents the mean travel time residual over several perforation shots for that particular receiver, calculated by taking the difference between observed and modelled traveltimes $T_{obs} - T_{mod}$.

(a) VTI calibration residuals

Receiver	Δt_P [ms]	Δt_{Sh} [ms]	Δt_{Sv} [ms]
pos. 1 rec. 1	0.5	-2.9	-1.4
pos. 1 rec. 2	0.7	-2.0	-1.0
pos. 1 rec. 3	0.8	-2.0	-0.7
pos. 1 rec. 4	0.8	-2.0	0.3
pos. 1 rec. 5	0.3	0.1	0.0
pos. 1 rec. 6	0.0	-0.1	0.8
pos. 1 rec. 7	-0.6	1.1	0.2
pos. 1 rec. 8	-1.0	-0.2	1.1
pos. 1 RMS	0.7	1.6	0.8

3-3 Velocity Model Testing

A closer examination of Becker (2015)'s traveltime residuals -the difference between observed and modelled arrival times $T_{obs} - T_{mod}$ - from the model calibration displays systematic biases that correlate with the horizontal angle of wave propagation. In figure 3-4, one can see that when raypaths are less perpendicular to the receiver set, the absolute value of the traveltime residuals increases. Since P-wave traveltime residuals for perforation shots in wells 4H, 10H and 11H (figure 1-4) range between -8 ms and 3 ms, there is no reason to believe that traveltime residuals increase with increasing distance. Hence I hypothesise that this phenomenon is due to horizontal anisotropy not being accounted for in the VTI model. The HTI model corrects for this systematic bias, lowering the absolute value of the traveltime residuals for the 3 stages shown in figures 3-3 and 3-4.

Localisation of perforation shots is done to test the robustness of the velocity model and mapping method. By quantifying the difference in location between the mapped perforation shots and their true location, an idea of the robustness of the velocity model is obtained. Localisation was done by applying Coalescence Microseismic Mapping (as described in chapter 2) based on P-wave arrivals only with an STA/LTA detection threshold of 2. To calculate the STA/LTA ratio, a short window length of 16 ms and a long window length of 80 ms were maintained. Analogous to Becker (2015), localisation was improved by applying Geiger linearised least-squares travel time inversion (Geiger, 1910) for all but 3 perforation shots. Geiger inversion relies on P and Sh arrivals with directional information from hodograms (crossplots of two components of particle motion over a time window) calculated using the azimuth of P-waves. P-wave, S-wave onset times and azimuthal uncertainty were set at 2 ms, 4 ms, and 2 degrees respectively.

Figure 3-5 displays the difference in location error between the HTI and VTI models, which was calculated by $\frac{|l^{pred} - l^{true}|}{d_{sr}}$. l^{pred} represents the predicted location, l^{true} the true location and d_{sr} the source-receiver distance, measured from the true perforation shot location to the

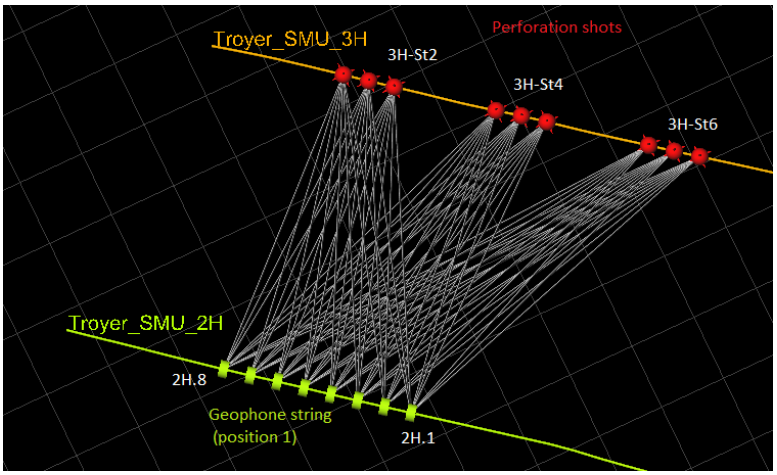

Figure 3-3: Overview of geophone toolstring 1 in well 2H with respect to perforation shots in stages 3H-St2, 3H-St4 and 3H-St6.

middle of the receiver array. Becker (2015) reported an increase in relative error with decreasing distance to the receiver with the VTI model (figure 3-5b). Such behavior is unexpected because an increase in source-receiver distance will attenuate the signal and therefore decrease the signal-to-noise ratio (SNR) (Aki and Richards, 1980).

Since the incidence angle is larger for the perforation shots in wells near the monitoring well (figure 3-4), this is likely the source of bias in the VTI residuals. The HTI model removes this angle-of-incidence bias and the relative location errors (with the normalisation by distance) do not depend on the source-receiver distance anymore. It should be noted that the final location error is a function of picking uncertainty, availability of P and S time picks, and inaccuracies in the velocity model related to geological heterogeneities. During the time picking stage, only the higher quality arrivals were considered for the model calibration. Therefore, availability of P and S time picks, and velocity model inaccuracies are dominantly responsible for the relative location errors.

3-4 Event Localisation

Event localisation was carried out by means of CMM. Then, Geiger event relocation for both HTI and VTI models was conducted with the same 12 x 12 x 6 m (40 x 40 x 20 ft) spaced 3D-grid. The analysed dataset counts 94 hydraulic fracturing stages, out of which 3 stages have been selected for detailed analysis. Geiger inversion parameters are based on P- and S-wave arrival times and hodograms of their directional (dip and azimuth) information. P- and S-wave onset time picks, and azimuthal uncertainty was maintained at 2 ms, 3ms and 2 degrees respectively. For the VTI model, Geiger relocation resulted in two layered clusters of events just above and below the boundaries of the target layer (following the velocity model). This clustering effect was identified as an artifact. For the HTI model, the microseismic clouds produced by CMM + Geiger relocation and CMM-only were almost identical. Therefore, for the sake of consistency, the results compared in this section are processed by means of CMM only. To ensure a minimum data quality of imaged events, filters were applied to the raw microseismic cloud (figures 3-6 and 3-7).

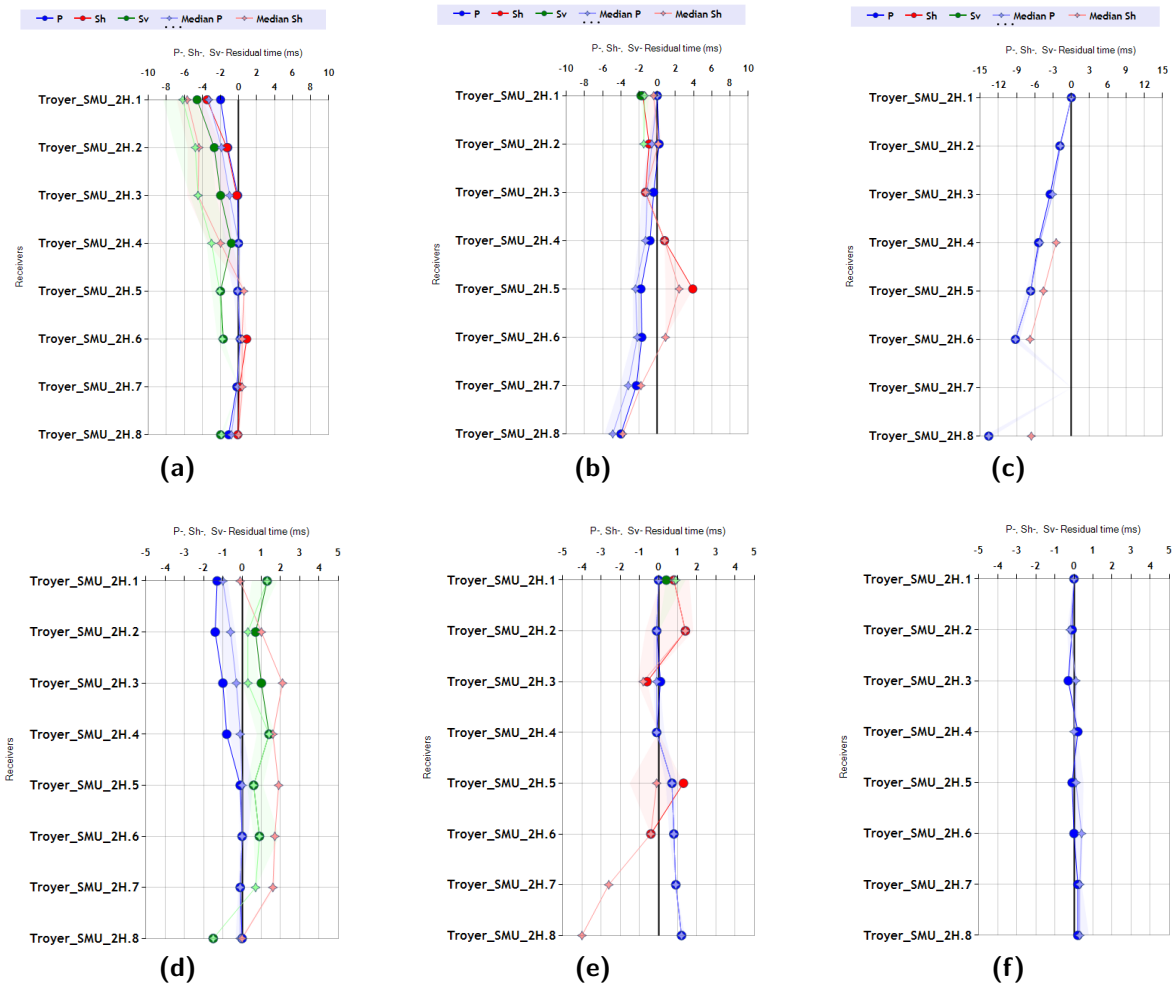

Figure 3-4: Traveltime residuals $T_{obs} - T_{mod}$ for the VTI velocity model in well 3H stage 2 (a), stage 4(b), stage 6 (c). Also, traveltime residuals for HTI model calibration in well 3H stage 2 (d), stage 4(e), stage 6 (f). The VTI residuals show systematic bias depending on their relative position to the geophone string. Note the difference in scale between the VTI and HTI traveltime residual plots.

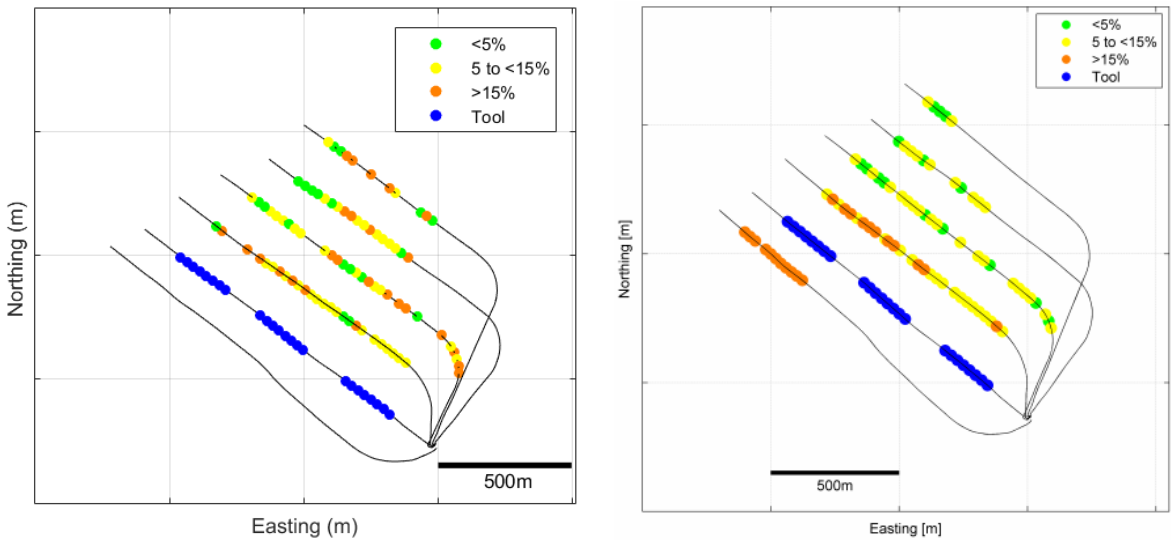

Figure 3-5: Colour-coded maps of the relative location error of perforation shots in the HTI model (a) and the VTI model (b). Blue dots denote the toolstring, the other dots represent perforation shot locations and their relative location error. The perforation shots in the well southwest of the monitoring well are not considered in the HTI calibration because this well penetrates a different geologic layer, violating the assumption of homogeneity in the velocity model.

An orthogonality filter was imposed because in theory, P- and S-wave arrivals are orthogonal to each other. In practice, the angle between P- and S-arrivals deviates from the expected 90° for various reasons such as superposition of waveforms in complex geology, low SNR, erroneous (automatic) phase picking or false event triggering. By demanding a minimum orthogonality of 0.70, a deviation up to 27° from the normal angle was tolerated.

For each microseismic event, an uncertainty ellipsoid is constructed by minimising the Chi-square statistic of the event location problem through:

$$\chi^2(x) = \sum_{l=1}^{2} \left[\sum_{i}^{N} \left(\frac{T_{il} - \tau_{il}}{\sigma_{Tl}} \right)^2 + \sum_{i}^{N} \left(\frac{\Theta_{il} - \theta_{il}}{\sigma_{\Theta l}} \right)^2 \right] \quad , \tag{3-4}$$

where l is the index of the P- ($l = 1$) and S-waves ($l = 2$), i is the index of the observation (receiver), N the number of observations, T_{il} and $\tau_{il} = \tau_{il}(x, y, z, t)$ are observed and computed onset times, Θ_{il} and $\theta_{il} = \theta_{il}(x, y, z, t)$ are observed and computed polarisation angles respectively. σ_{Tl} and $\sigma_{\Theta l}$ are the standard deviations of observed onset times and polarisation angles respectively. Note that the uncertainty ellipsoid is taking into account both onset times ***and*** polarisation angle. In the literature (e.g. Eisner et al., 2009; Mueller et al., 2011; Li et al., 2014), location uncertainty is calculated in a variety of ways, and often depends only on onset times, so care should be taken when comparing values reported by different authors. The maximum length of the longest axis of the uncertainty ellipsoid was set to be smaller than 150 m.

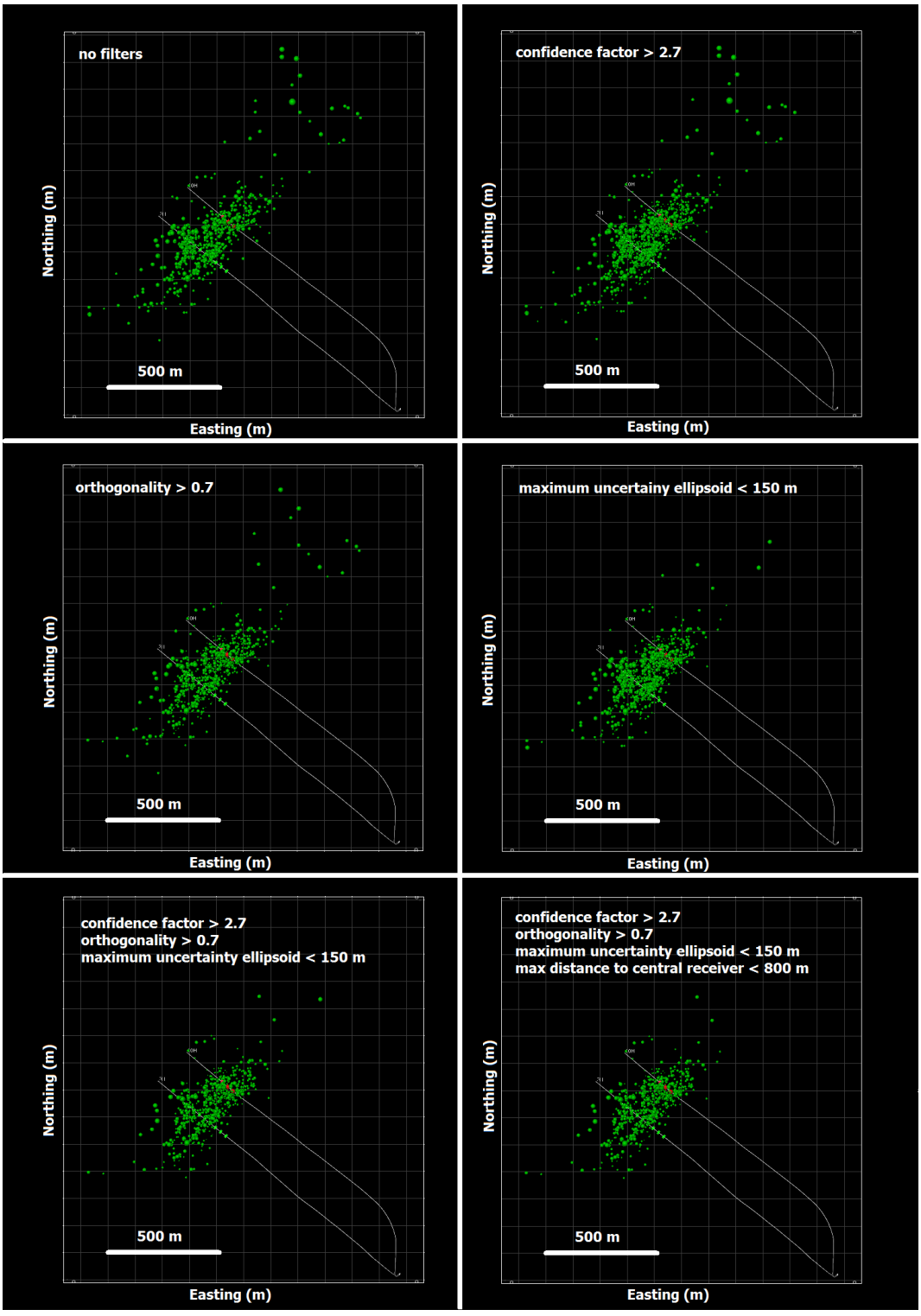

Figure 3-6: Display of the effect of different filters (see text for explanation) on HTI processed data of fracking stage 10H3. The distance filter is justified by the poor quality of waveforms far away from the receiver, which causes the CMM algorithm to mispick the first arrivals. It should be noted that very few microseismic events are removed by this filter. Light green cylinders denote receivers, red dots denote perforation shot locations.

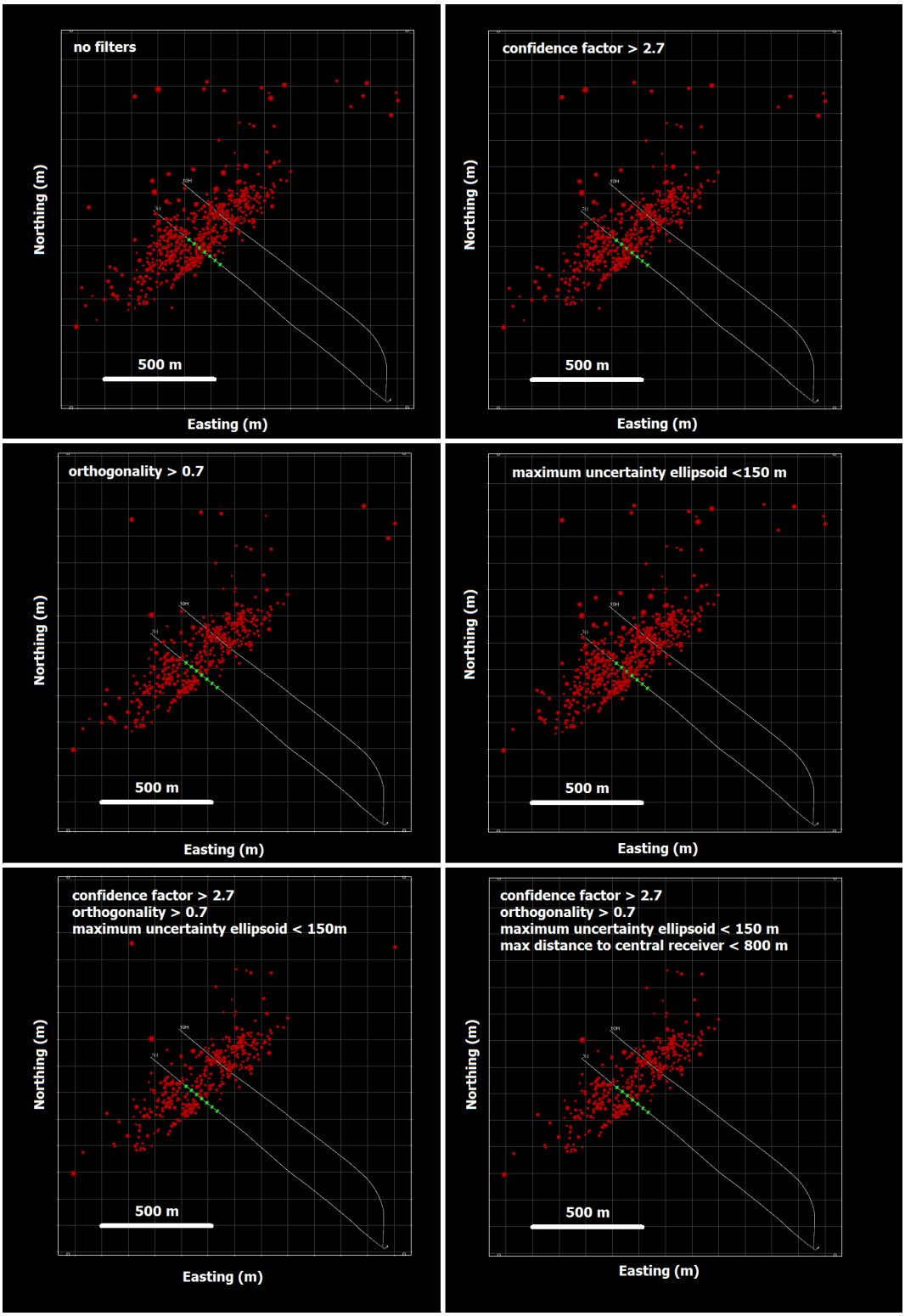

Figure 3-7: Display of the effect of different filters (see text for explanation) on VTI processed data of fracking stage 10H3. The distance filter is justified by the poor quality of waveforms far away from the receiver, which causes the CMM algorithm to mispick the first arrivals. It should be noted that very few microseismic events are removed by this filter. Light green cylinders denote receivers.

Confidence factor pertains to the sum of five quality control attributes, namely: P- and S-wave trace quality, P- and S-wave time pick residual magnitude and a general polarisation quality. Each quality control attribute is a normalised ratio of waveform attributes, expressed as a value between 0 and 1. A confidence factor of 2.7 was maintained, which means that the average individual quality attribute is likely higher than 0.5.

The distance filter is justified by the relatively high mis-pick rate that is observed beyond 800 m distance from the central receiver, which is due to a reduction in the SNR. The ideal course of action would be to manually repick every single microseismic event where possible, and discard events that cannot be manually repicked. However, in most cases, the poor quality of traces makes manual repicking challenging (figure 3-8). Furthermore, time constraints render manual repicking beyond the scope of this thesis. The choice was made to filter out most invalid events at the cost of also filtering out a few valid events. This approach does not compromise the matching of results with the surface processing locations because only the higher magnitude events (higher SNR) are expected to be detected from both arrays.

Figures 3-9 and 3-10 display the differences between the microseismic clouds of the HTI and VTI velocity models. The HTI model locates more events closer to the receivers than the VTI model. As observed with the perforations, the closer an event is to the array, the larger is the deviation of the angle of arrival from the perpendicular to the array. While the VTI model is unable to fit the travel time move-out introduced by the horizontal anisotropy, the HTI model does incorporate the azimuthal velocity variation and therefore collapses the arrivals producing an event location.

The average magnitude of the events in the HTI model is about 0.2 - 0.5 magnitude units larger than those in the VTI model (table 3-4). Since the spectral estimate of the magnitude depends on the velocity (equations 2-1 and 2-2), this increment is to be expected.

Table 3-4: Average magnitude of microseismic events for each stage and velocity model.

	HTI	VTI
10H3	-1.46	-1.91
10H4	-1.38	-1.88
10H5	-1.29	-1.47

Another interesting feature is the difference in 'trend angle' of the microseismic event cloud. The HTI clouds seem to be more perpendicular to the direction of the wells than the VTI clouds. Neither trend angle aligns with the direction of the look-up-table (displayed by gray dashed lines), which means that this is a genuine feature of the microseismic cloud. The azimuthally varying velocity in the HTI model could be a possible explanation for this difference. If the HTI model corrects appropriately for horizontal symmetry and the microseismic events lie in a perfectly linear plane, then the VTI microseismic cloud is expected to show some degree of curvature. In the VTI microseismic cloud of stage 10H4 (figure 3-9), a slight curvature can be observed. However, since the microseismic events are not guaranteed to align linearly, and the observed curvature is still within the margin of interpretation, this observation cannot be used as evidence for the hypothesis.

Going through the stages one by one, one can see that in stage 10H3 both HTI and VTI bring out two similar linear features that can be interpreted as seismic events along a hydraulic fracture. HTI leaves room for the interpretation of a third linear feature to the northwest of,

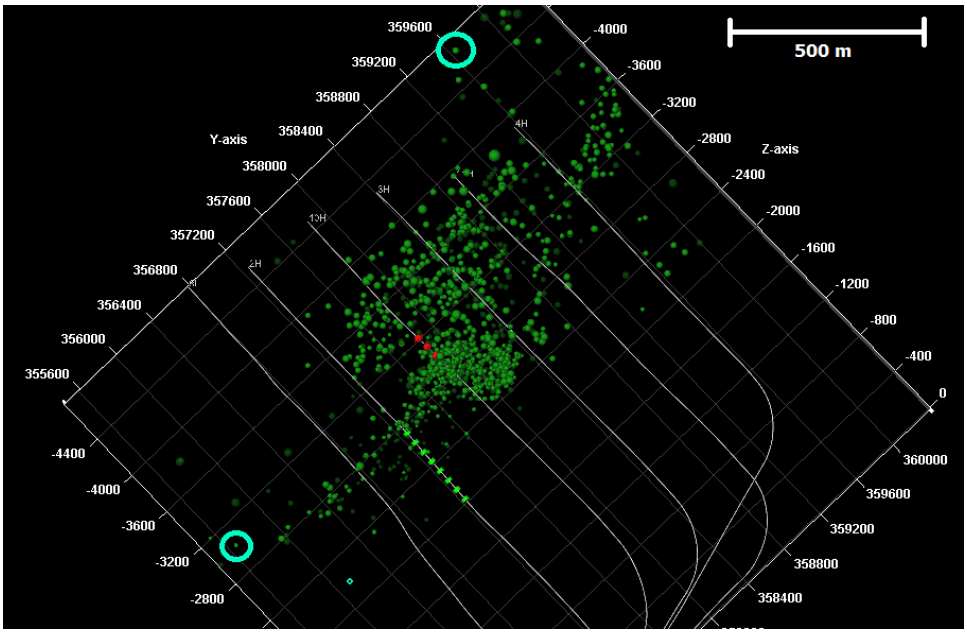

(a) Overview of microseismic events during fracking stage 10H5. Green circles indicate the events whose waveforms are displayed below. Filters applied: confidence factor ≥ 2.7, orthogonality ≥ 0.7, maximum uncertainty ellipsoid ≤ 150 m, no distance filter.

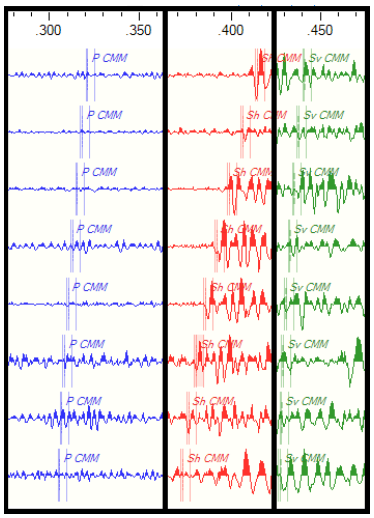

(b)

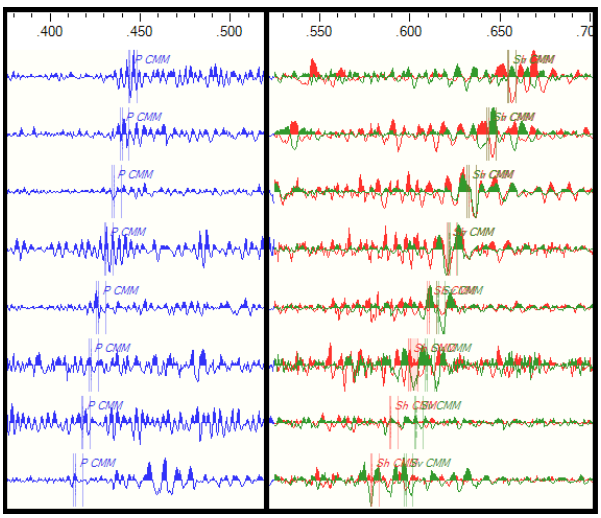

(c)

Figure 3-8: Automatic first break picking for events far away from the well. The farther away from the well (lower SNR) the more difficult the first breaks can be distinguished. CMM picks are incorrect on traces with a complex trail of arrivals. (b) Lower-left event in (a): P-wave arrivals are picked in locations where there is clearly no P-wave arrival, Sh-wave arrival is picked reasonably well, Sv-wave arrivals cannot be distinguished due to high noise levels. (c) Upper-middle event in (a): the picked P-wave arrivals are highly dubious, Sv- and Sh- first breaks are picked coincidentally.

and parallel to, the other two linear features. In stage 10H4, both models again bring out two linear features, where the VTI model exhibits a slightly stricter delineation. The microseismic events of stage 10H5 merely show a myriad of events close to the perforation shot, but the HTI also seems to pick up a linear feature southwest of, and perpendicular to the receiver set.

A vertical display of the microseismic HTI and VTI clouds (figure 3-10) reveals that the VTI result is much better constrained in depth and that microseismicity is constrained to the target layer. Figure 3-11 shows that within the target layer, the microseismic events seem evenly distributed in height and not migrated to either upper or lower layer boundaries. However, upon zooming in even further on the VTI depth plot, we can identify a slight staircase-type inclined structure, which is thought to be an artefact (Figure 3-12 (a)). Again, we identify a slight picking error for events on the fringe (figure 3-12).

The difference in vertical constraint is attributed to the VTI model taking into account the high velocity contrasts at the top and bottom of the target layer. These contrasts are what keep the locations within the target layer, since there is almost no vertical aperture to the receiver array in the horizontal well to help constrain depth. Without these contrasts, the locations obtained with the homogeneous HTI model suffer from the limitations of the monitoring geometry. Ultimately, it is the vertical constraint that is desired from downhole seismic data to help constrain the depth estimations in the processing of the surface recordings. By this criterion, VTI is the favoured velocity model. Nonetheless, the HTI model seems to improve localisation in the horizontal plane. The next level of complexity to test the improvement in event location would be to generate an orthorhombic model. This line of investigation, however, is outside the main goal of this thesis.

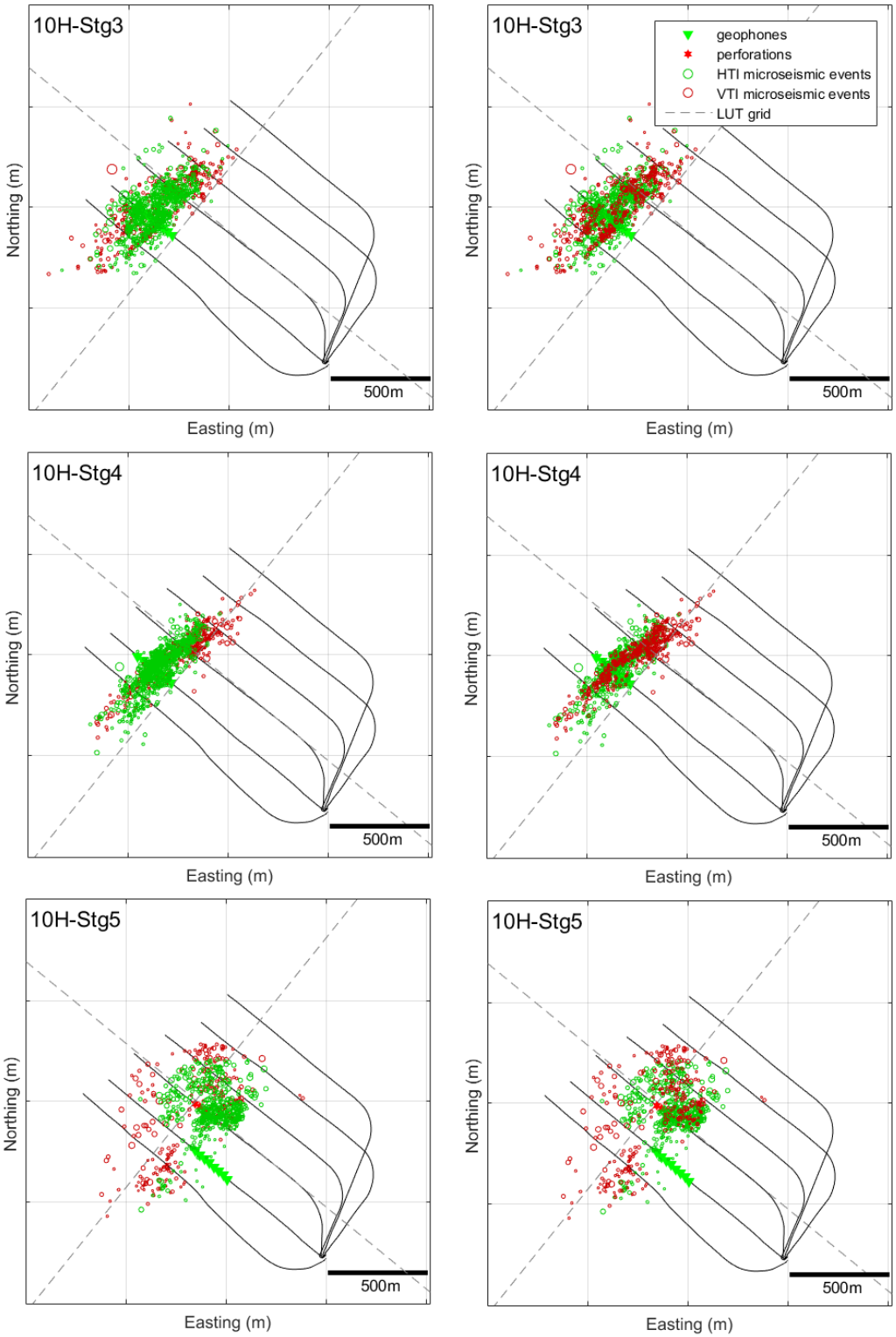

Figure 3-9: Comparison between event locations with HTI and VTI velocity models, both processed with the same sequence and same grid size. On the left HTI (green) overlies VTI (red), on the right VTI overlies HTI. The size of the circles scales with event magnitude. Filters applied: confidence factor ≥ 2.7, orthogonality ≥ 0.7, maximum uncertainty ellipsoid ≤ 150 m, maximum distance to receiver ≤ 800 m.

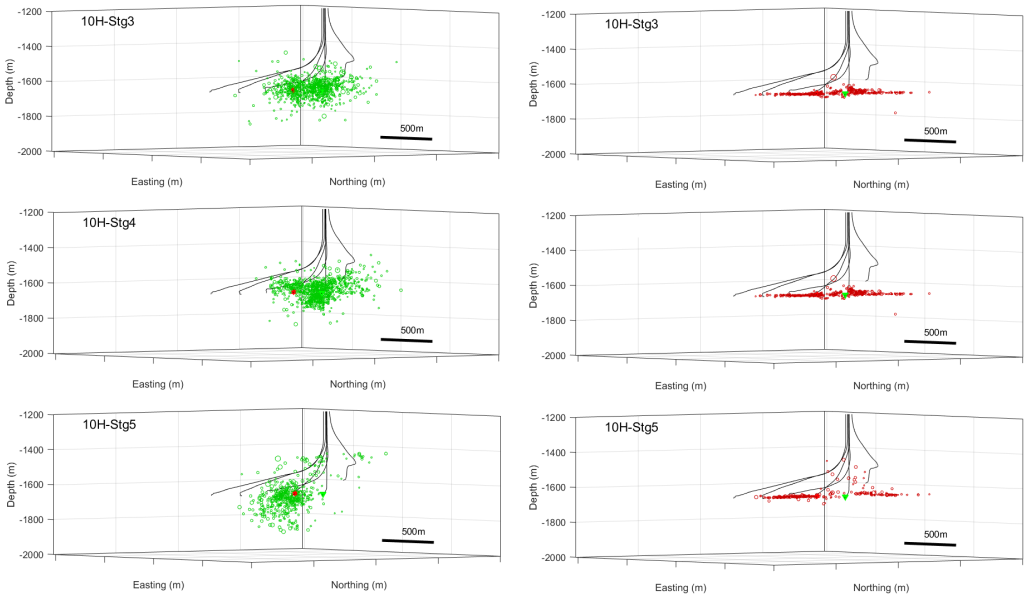

Figure 3-10: Comparison between event locations with HTI and VTI velocity models, both processed with the same sequence and same grid size. HTI is depicted in green on the left, VTI is depicted in red on the right. The size of the circles scales with event magnitude. Filters applied: confidence factor $\geq$ 2.7, orthogonality $\geq$ 0.7, maximum uncertainty ellipsoid $\leq$ 150 m, maximum distance to receiver $\leq$ 800 m.

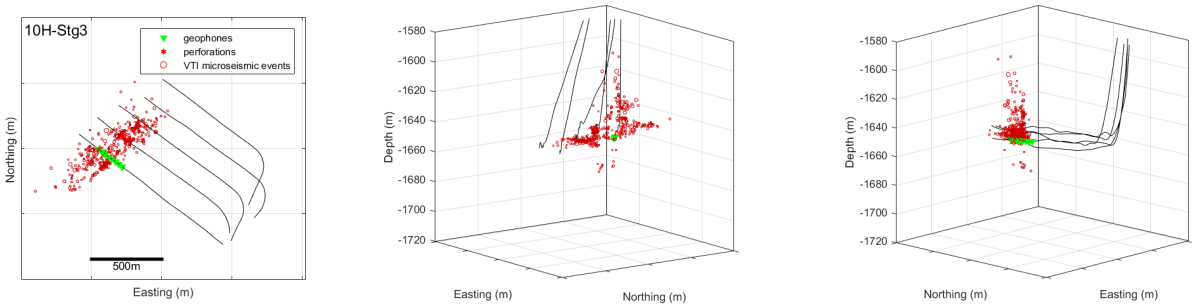

(a) **(b)** **(c)**

Figure 3-11: Zoomed in plot of microseismic stage 10H4, showing top view (a), northwest view (b), and southwest view (c), respectively. Note the slight gradient in the microseismic (best seen in image a): The depth of a seismic event is usually closest to the depth of the nearest well.

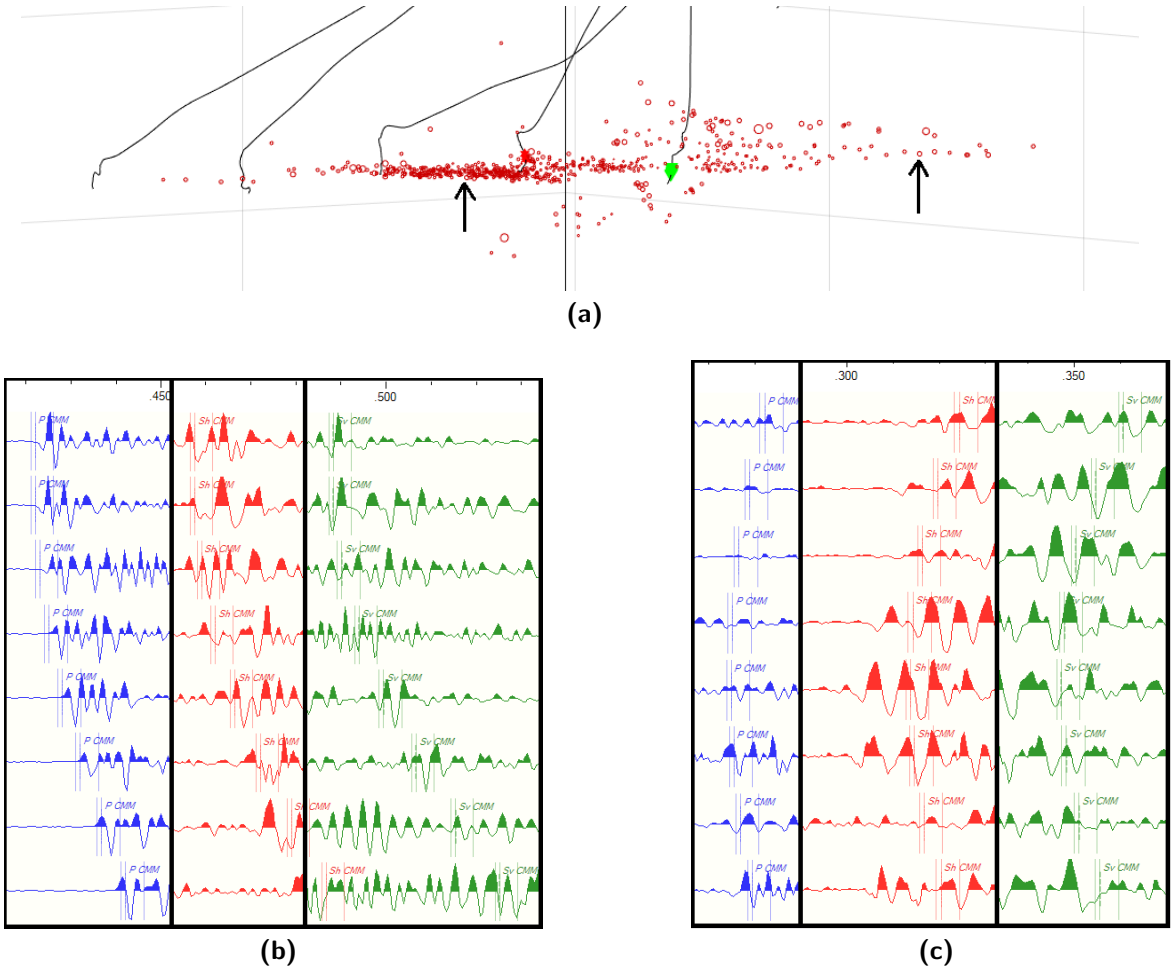

Figure 3-12: (a) Overview of VTI microseismic events during fracking stage 10H4. CMM time picks in (b) event with correctly identified arrivals (left arrow in (a), reliable event location), and (c) event with misidentified arrivals (right arrow in (a), location with higher uncertainty).

Chapter 4

Event Location from Surface Data

Surface microseismic monitoring complements downhole seismic monitoring in a number of ways. The large aperture of arrays in surface monitoring is ideal to localise the horizontal position of microseismic events. Furthermore, event locations derived from surface passive seismic are not very sensitive to the velocity model that is used (Grechka et al., 2015). However, because S-waves are highly affected by geological hetereogeneities and near-surface attenuation (Kolinsky et al., 2009), they are visible on the largest events only (Duncan and Eisner, 2010a), and difficult to use for depth determination. Generally, only P-wave information is used for surface microseismic processing. Therefore, surface monitoring suffers from uncertainty in the vertical direction, while downhole data offer good constraints for depth determination. This chapter will first discuss the processing sequence used in surface monitoring and then focus on the complementary aspects of surface and downhole seismic monitoring.

4-1 Monitoring Setup and Velocity Model

Surface acquisition was made using 1082, 1-component Geospace Seismic Recorder geophones laid out in 10 lines in a frac-star array configuration. The geometry of the lines was dictated by environmental constraints (figure 4-1). An average receiver separation of 25 m and a sampling rate of 2 ms were maintained throughout the acquisition. In total, 435 hours of surface recordings were acquired which included all 94 fracking stages. The dataset was processed using a homogeneous velocity model exhibiting a vertical P-wave velocity of 5500 m/s.

4-2 Conditioning and Processing

A sequence of signal processing techniques proposed by Gendrin et al. (2016) was used to condition and process the raw surface recordings, following the scheme in figure 4-2.

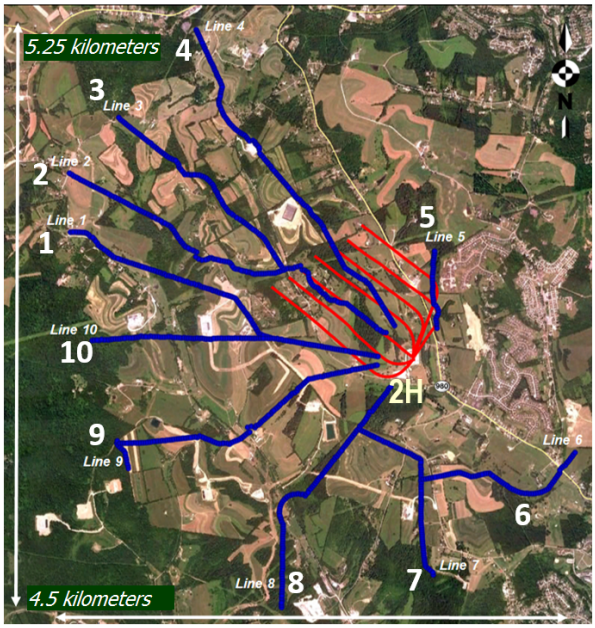

Figure 4-1: Areal view of monitoring site. Blue lines denote seismic arrays. Modified from (Bradford et al., 2013).

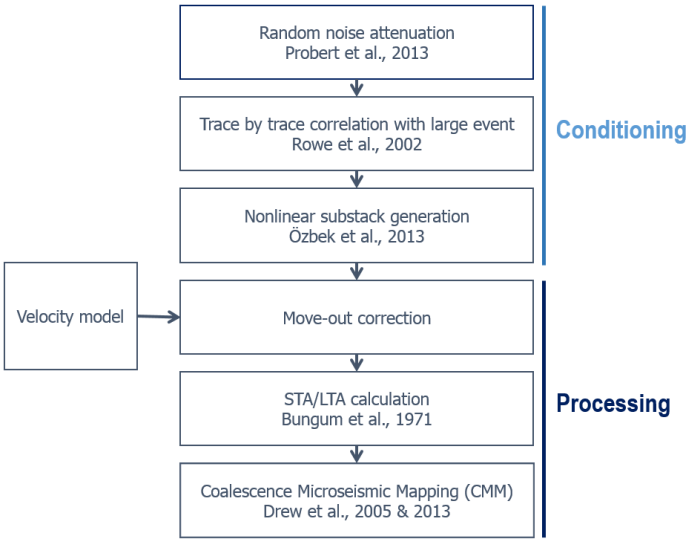

Figure 4-2: The conditioning and processing sequence that was followed for processing surface seismic data. Adapted from Schlumberger presentation at EAGE conference 2016 in Vienna (Gendrin et al., 2016).

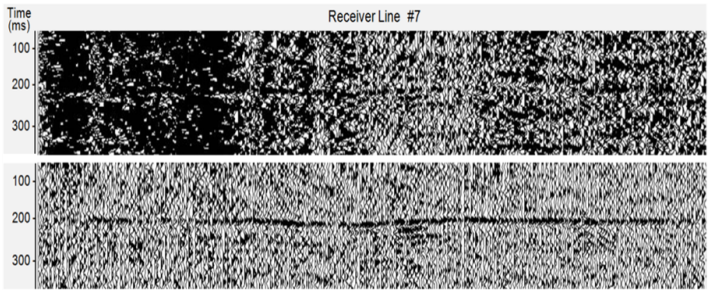

Figure 4-3: Top: pre-processed signal of perforation shot, line shows average data quality. Bottom: same data after random noise attenuation. Adopted from Probert et al. (2013).

The first step in the processing sequence consists in whitening the frequency spectrum of the data to attenuate random noise (Figure 4-3). Noise whitening works trace by trace without requiring any a priori knowledge about the properties of the medium of propagation. This processing step is also common in the processing of reflection seismology data. The details of the algorithm used in this thesis can be found in Probert et al. (2013) and Gendrin et al. (2016).

The second processing step in the workflow consists in the correlation of the data with the observations of a high SNR reference event (Rowe et al., 2002). The cross-correlation helps to detect events in lower SNR conditions provided that the location and source mechanism are similar to the reference event. The cross correlation also reduces the dependency on the velocity model to estimate event locations rendering accurate relative locations with respect to the reference event. This processing step results in a significant boost in the number of detected and located events as it helps to overcome important limitations related to an incomplete knowledge of the source signature and the velocity model (e.g., static corrections, anisotropy, heterogeneity). Figure 4-4 displays the improvement that the cross-correlation has on the STA/LTA ratios and CMM peak.

Phase-weighted n-th root nonlinear stacking was applied following Özbek et al. (2013). The method is a combination of n-th root (NR) stack for L traces (Kanasewich et al., 1973)

$$y_{NR}(t,n) = sgn[u(t,n)]\,|u(t,n)|^n\,, \quad \text{where} \quad u(t,n) = \frac{1}{L}\sum_{i=1}^{L} sgn[x_i(t)]\,|x_i(t)|^{1/n}\,, \tag{4-1}$$

and phase-weighted (PW) stacking proposed by Schimmel and Paulssen (1997)

$$y_{PW}(t,m) = [y_p(t)]^m \frac{1}{L}\sum_{i=1}^{L} x_i(t), \quad \text{where} \quad y_p(t) = \frac{1}{L}\left|\sum_{i=1}^{L} exp\left\{j\phi_{x,i}(t)\right\}\right| \tag{4-2}$$

is the phase stack derived from the instantaneous phase of the analytical signal $x(t)$. The phase-weighted n-th root (PWNR) stack is defined as:

$$y_{PWNR}(t,m) = [y_p(t)]^m y_{NR}(t,n) \tag{4-3}$$

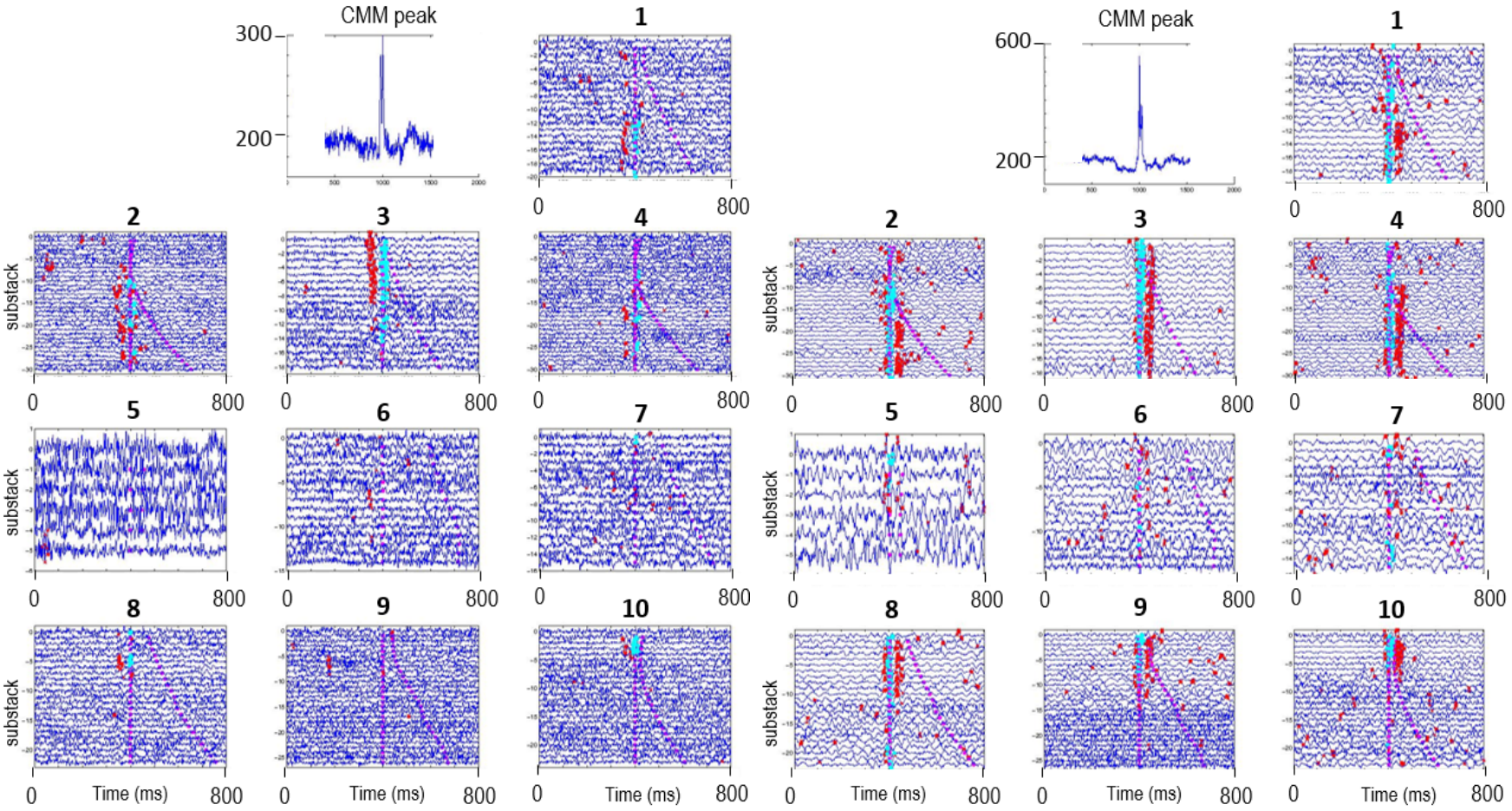

(a) Before cross-correlation with large event.

(b) After cross-correlation with large event.

Figure 4-4: Improvement in SNR of 10 substacks that contribute to a CMM peak before and after cross-correlation with a large event. Blue represents the traces, red dots denotes high STA/LTA, cyan dots denotes high STA/LTA around P-arrival, magenta denotes the move-out. Modified from (Gendrin et al., 2016).

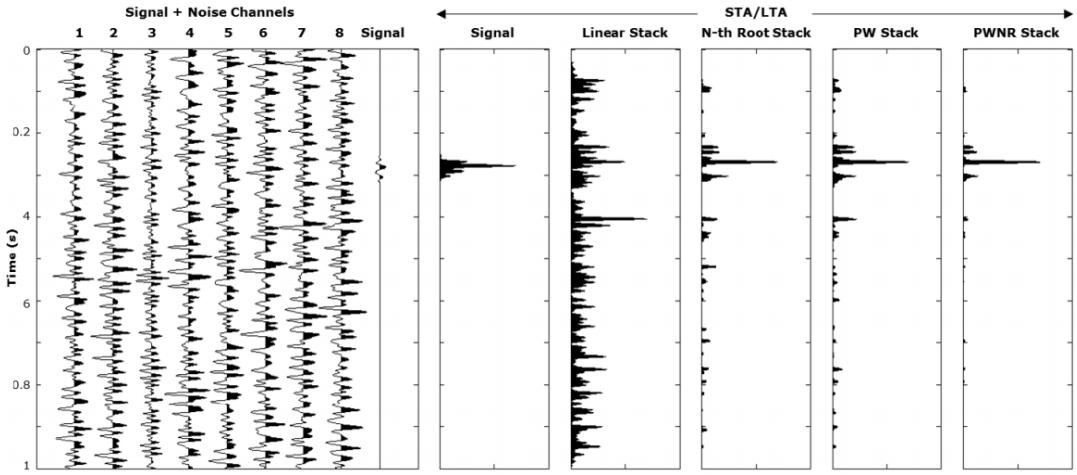

Figure 4-5: Left: Eight noise traces with signal added at 0.3 sec with SNR of -13 dB. Channel 9 shows underlying signal. Right: STA/LTA detection function applied to the signal, the linear stack, the n-th root stack, the phase-weighted stack and the phase weighted n-th root stack. Adopted from (Özbek et al., 2013).

m (usually $\sim$2 or $\sim$4) and n (usually $\sim$2) are variables that a geophysicist can use to optimise the SNR. The effect of the PWNR nonlinear stack can be seen in figure 4-5.

The processing sequence of the pre-conditioned seismic data into maximum-likelihood event locations with corresponding CMM cubes was the same as for the downhole processing. First a move-out correction was applied, using a look-up-table (LUT) approach with a grid spacing of 6.5 meters (20 ft). Subsequently, the STA/LTA ratio was calculated for each trace to detect microseismic events. Lastly, coalescence microseismic mapping (Drew et al., 2013) was carried out, also with a 6.5 meter-spaced LUT.

4-3 Event Localisation

Since seismic waves generated by microseismic events have to travel farther (compared to downhole) to the receivers, a lot of wave energy is attenuated by the time they arrive at the receiver, which results in weak arrivals. As a consequence, only the higher magnitude events can be detected with surface arrays (Van Renterghem et al., 2015). Due to the attenuation from the overburden, only frequencies below 80 Hz (or at the utmost 100 Hz) are measured at the surface. Unfortunately, this does not allow the determination of the event quality attributes that were used to QC (quality control) the downhole arrivals. The clear linear structures in the surface recorded microseismic cloud of events gives confidence in the identification of actual microseismic events, and not just false triggers. In order to be able to compare the surface microseismic cloud of events to downhole microseismic cloud of events, it is important that the difference in sensitivity of each method is corrected for. Event clouds with similar relative magnitudes should be compared because the same microseismic events are being imaged.

Because event magnitude is one of the waveform attributes whose derivation is controversial for surface microseismic data (Eisner et al., 2013, 2014; Morozov et al., 2014), we plot the

CMM peak -an expression of signal strength- instead of the magnitude. It is beyond the scope of this thesis to derive an empirical relationship between magnitude and CMM peak. The minimum detectable magnitude corresponding to the surface data was therefore determined by visually comparing the number of microseismic events of the surface microseismic cloud to the number of events in the downhole microseismic clouds. It was found that a threshold of $magnitude \geq -1.75$ resulted in comparable microseismic clouds of events between downhole HTI and surface. For VTI, the threshold was lowered using the difference in average magnitude between HTI and VTI as depicted in table 3-4 (0.45 for 10H3, 0.50 for 10H4 and 0.18 for 10H5).

When we look at the uppermost plots of figures 4-6, 4-7 and 4-8 it can be seen that surface microseismic monitoring does indeed constrain appropriately microseismic event locations in an X-Y plane. This observation is based on the event locations of all 94 stages. Stages 10H3, 10H4 and 10H5 all show clear linear features that can be interpreted as activated fractures along a hydraulic fracture plane. When comparing downhole HTI microseismic clouds to surface microseismic clouds, it can be seen that for stage 10H3 both methods pick up three linear features, but at slightly different angles. For 10H4, the two methods detect the same linear feature, but the HTI cloud is denser and less elongated. For 10H5, both methods pick up a lot of seismic activity around the perforation shot, and each method picks up a different elongated feature, possibly complementary.

When comparing downhole VTI and surface microseismic clouds of events, one can see that for stage 10H3, on the southwestern side of the receivers, VTI and surface results are nearly one-on-one comparable, while on the northeastern side, VTI shows activity in areas where surface does not. For stage 10H4, VTI displays the same linear features as surface albeit slightly shifted to the southeast, akin to the HTI cloud. Besides higher activity around the perforation shot, stage 10H5 does not display strong similarity between both methods. Additionally, for suspicious event locations, picks should be checked and repicked if necessary, but in this thesis we focus on automatic processing only. All in all it seems that VTI shows greater similarity to surface event locations than HTI, but HTI does pick up microseismic events in areas that can complement and influence the interpretation of vague suspected features of surface microseismic clouds.

In terms of depth confinement, surface recorded microseismic events range in an interval of 60 meters around the target layer (figure 4-9). Interestingly, surface monitoring does seem to pick up the slight dip of the reservoir, despite its poor constraint in vertical direction. On the right side of figure 4-9, VTI depth confinement is displayed in red to demonstrate the potential of a joint location effort.

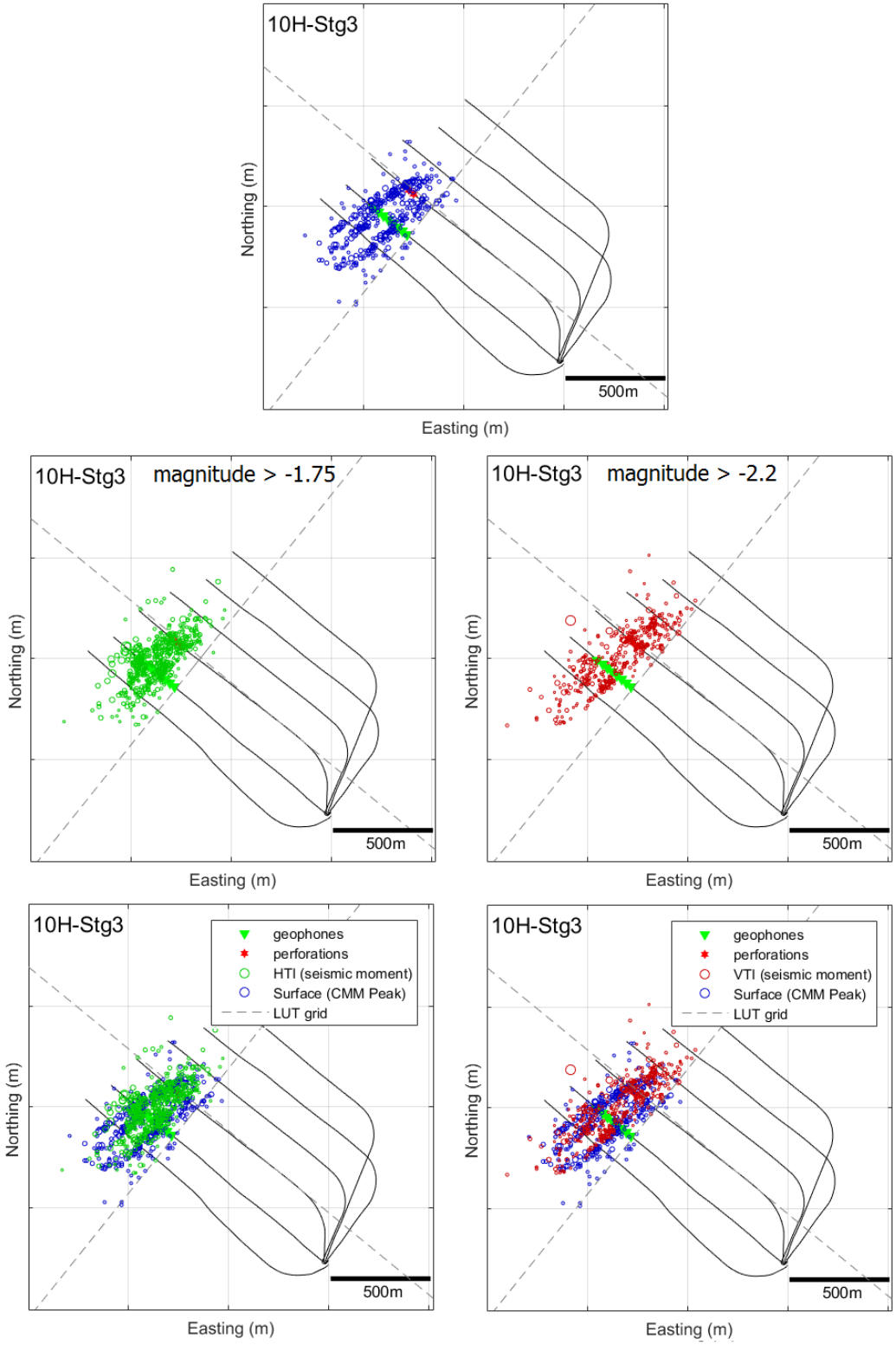

Figure 4-6: Comparison between event locations with surface (blue) and downhole (HTI in green, VTI in red) for stage 10H3. HTI microseismic cloud displays clearer distinct features, VTI microseismic cloud matches better with surface-monitored events than HTI.

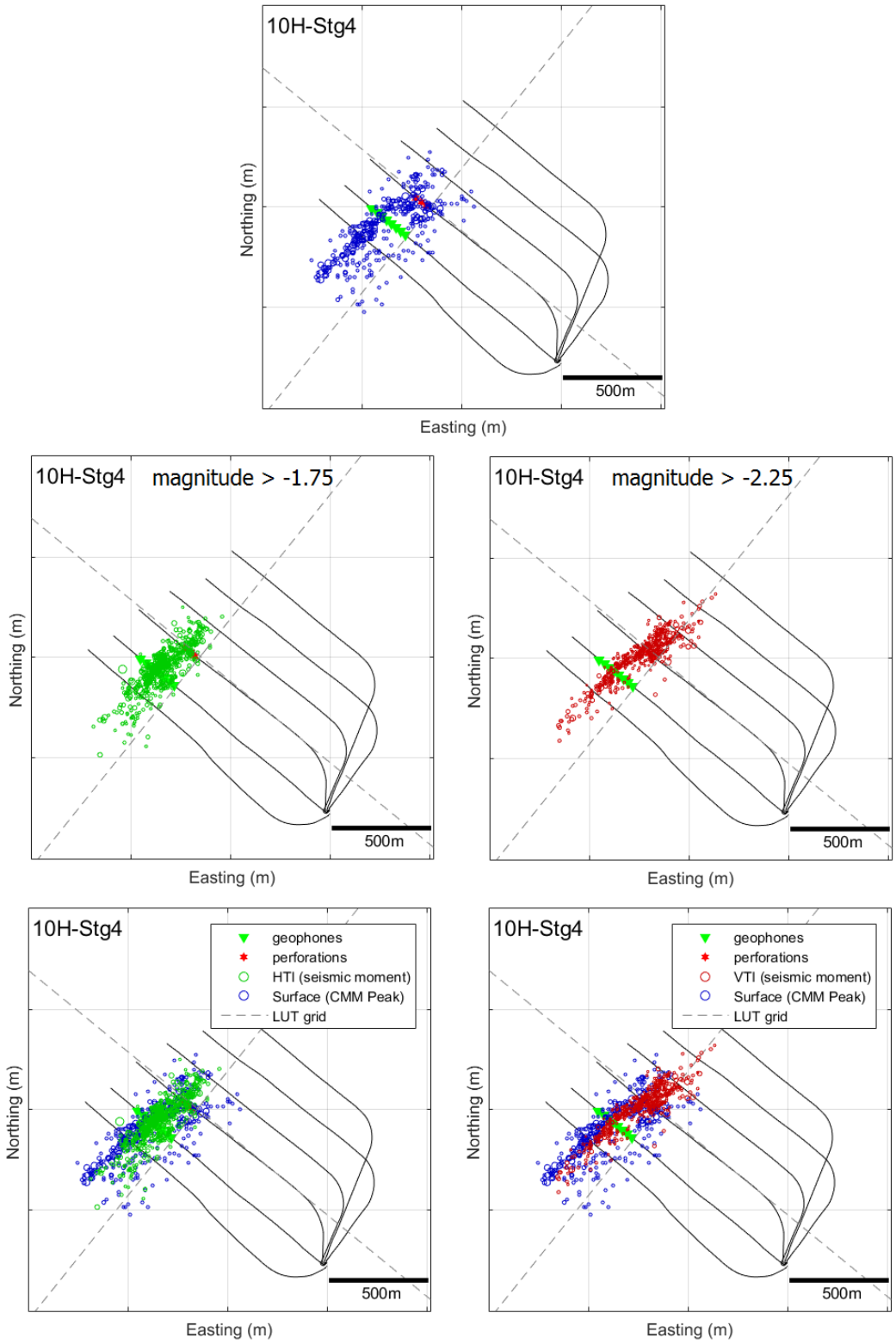

Figure 4-7: Comparison between event locations with surface (blue) and downhole (HTI in green, VTI in red) for stage 10H4. HTI and VTI models both locate the microseismic events slightly more towards the southeast compared to the surface microseismic events.

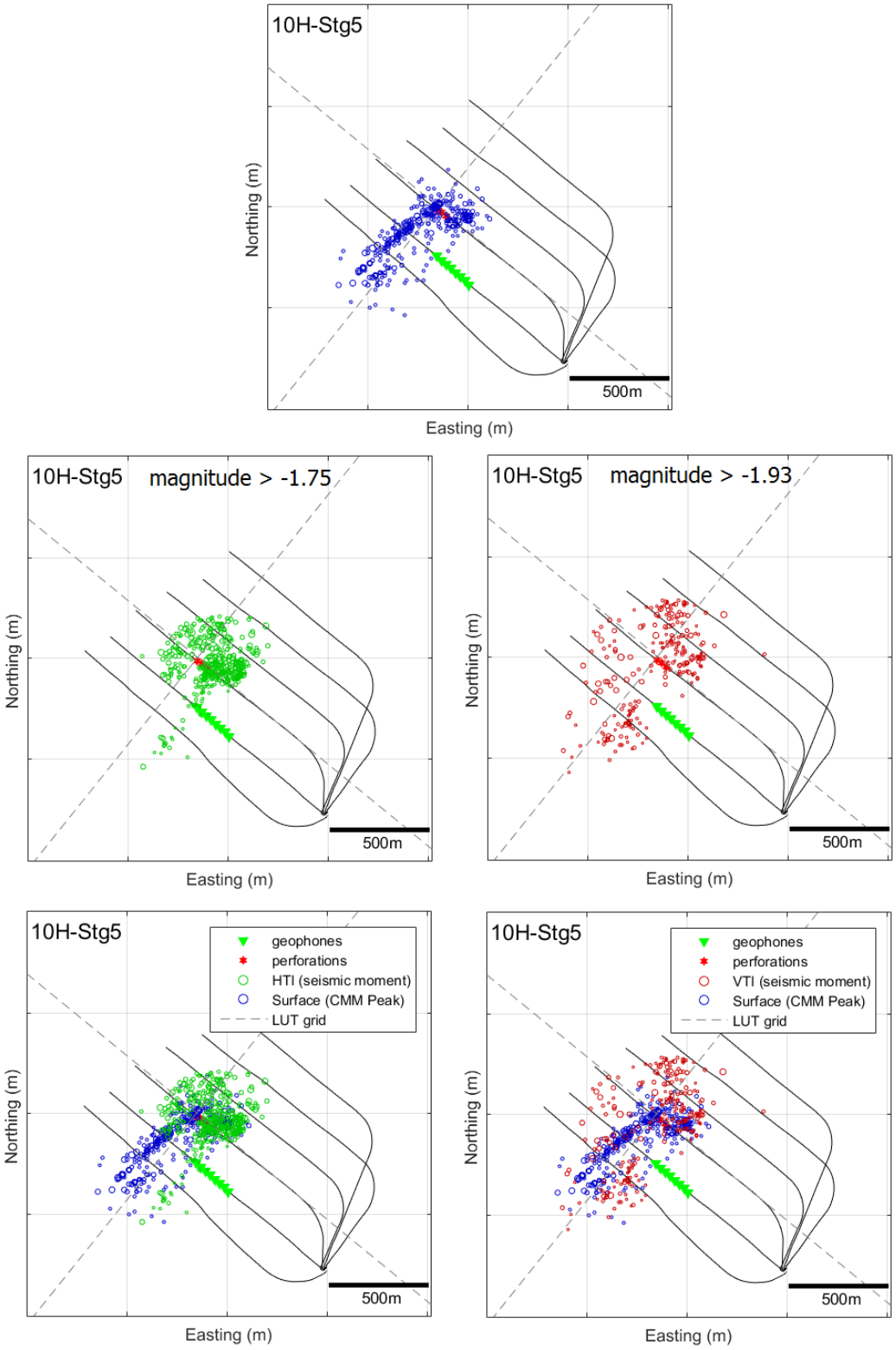

Figure 4-8: Comparison between event locations with surface (blue) and downhole (HTI in green, VTI in red) for stage 10H5. All methods show high microseismic activity around the perforation shot. Surface and HTI distinguish different linear features on the southeastern side of the array. Please note the relatively high angle between source and receiver in this stage, which distorts the arrivals for VTI, as explained in figure 3-4.

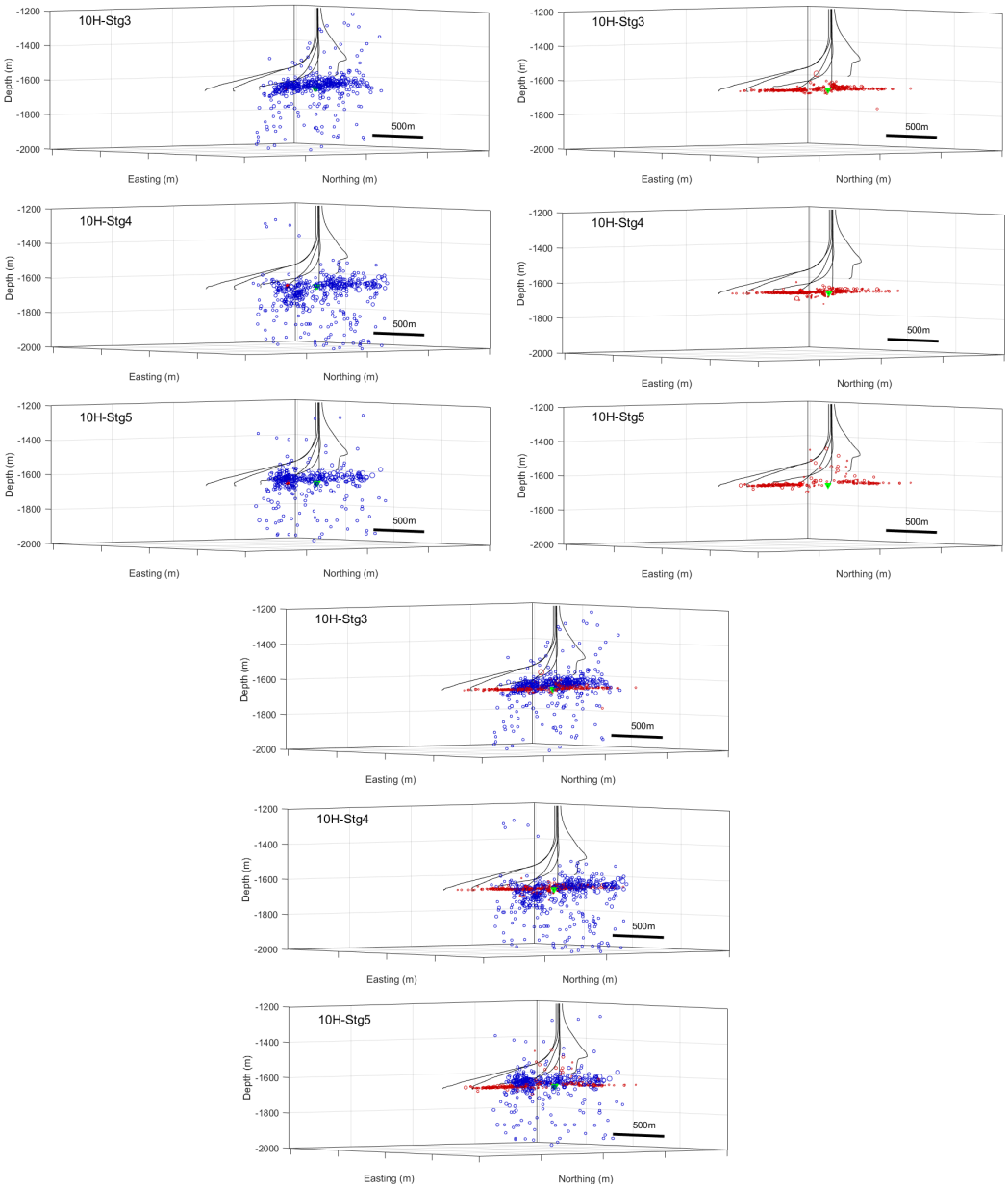

Figure 4-9: Vertical constraint comparison between surface monitoring microseismic locations on the left (blue) and downhole VTI microseismic locations on the right (red). Bottom: overlay of the two top displays. Note the dipping trend of the surface microseismic clouds.

Chapter 5

Joint Inversion

The goal of combining surface and downhole data for microseismic event location is to obtain a more accurate and less ambiguous estimate than obtained by inverting such datasets independently, by capitalising on the individual separate strengths of surface and downhole monitoring. Surface monitoring yielded CMM cubes (four-dimensional pdfs, see chapter 2.3) that constrain the microseismic event location estimate well in the horizontal plane, but not so much in the vertical direction. CMM cubes derived from downhole VTI recordings provided adequate constraint on the vertical location of each event, but display greater uncertainty in the X-Y direction. In this chapter, these complementary benefits are integrated in a joint location effort by matching surface and downhole detections in time and space, followed by a multiplication of the CMM cubes.

5-1 Time Matching

Because the travelpaths from the microseismic event to the downhole receivers and to the surface array are different, and the focal coverage of the monitoring arrays is also distinct, seismic events that are detected with one array, may not be detected by the other array because of wave energy attenuation and radiation pattern effects. In other words, it is not given that all events detected with the downhole array will have a reciprocal detection in the surface recordings, and vice versa. In general, the number of detected events is much larger in the downhole dataset, and hence the number of events that can be jointly located is mainly constrained by the number of events detected with the surface array. A lag was observed between downhole and surface origin time estimations that varied from $\sim$0.5 s in stage 10H3 to $\sim$1.5 s in stages 10H4 and 10H5. A lag on the order of 0.5 to 1 s was expected because the time of the first sample in the data files was rounded to the nearest second. Smaller discrepancies in origin time on the order of a few tens of milliseconds were also expected as a result of differences in event location and the use of effective velocity models. The lag has been corrected for by applying a bulk shift, such that the median event lag is minimised. Figure 5-1 displays the result of time matching for stage 10H3, the results for stages 10H4 and 10H5 can be found in appendix A-1.

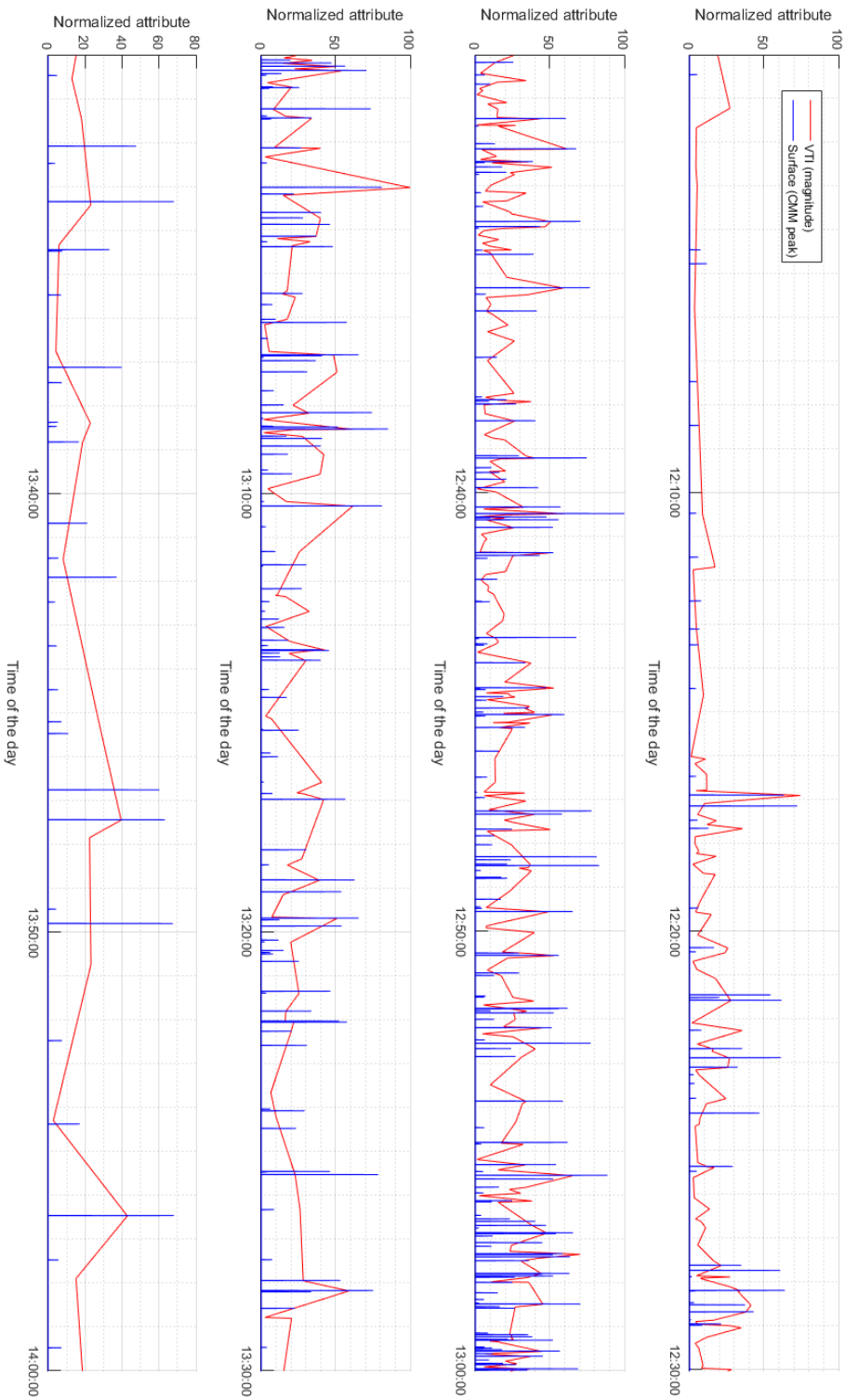

Figure 5-1: Results of a time match between VTI downhole and surface microseismic detections for stage 10H3. Blue spikes represent surface array detections, kinks in the red line denote downhole array detections.

In figure 5-2 the timematches are quantified. When we look at the histograms, the bars approach zero for time differences larger than 70 ms, coincidental detections within this time frame are considered a match. The limiting value of 70 ms was selected arbitrarily allowing differences in origin time of a few tens of milliseconds (see above for explanation), but also trying to maximise the number of events that could be matched. Nevertheless, most of the selected events fall within the interval from -20 to 20 ms (see figure 5-2). For stages 10H3 and 10H4, close to 40% of the events were matched in time. For stage 10H5, a quarter of events were matched in time.
As explained in chapter 2, the CMM cube is a four-dimensional probability distribution function, which can be broken down into a discrete time window with a three-dimensional (spatial) pdf for each timestep. The time matches in figure 5-2 refer to the time of maximum likelihood for the origin time of the event. Selecting an appropriate time window and sampling rate depends on the contributing signals and the spatial variation in modelled times, which are in turn governed by geometry and velocity (Drew et al., 2013). When locating events, we are mainly interested in finding the maximum likelihood position in all of the discrete time CMM cubes within the detection window. An appropriate initial upper limit of the time window is established by taking the time it takes to travel along the diagonal of a grid cell with dimensions $\Delta x \times \Delta y \times \Delta z$:

$$\Delta t_x = \frac{\sqrt{\Delta x^2 + \Delta y^2 + \Delta z^2}}{V_{min}} \tag{5-1}$$

which for our $12 \times 12 \times 6$ m grid, comes down to about 10 ms, assuming $V_{min} = V_s = 1786$ m/s. Some padding should be added as to not run the risk of under sampling, if the sampling rate is relatively large. The time window Δt_w is then narrowed down further using a type of octree search (Drew et al., 2013; Meagher, 1980). The optimal sampling rate can be derived from the variance σ_R^2 of the phase arrival pdf (Gaussian that fits the onset of the signal). Because $\sigma_R^2 = \sigma_D^2 + \sigma_G^2$ only depends on $\Delta t_{rms} = \sqrt{\sum (t_D - t_g)^2 / N}$, where σ_D^2 is the variance of a Gaussian fitting a maximum of the detection function, σ_G^2 is the variance of a Gaussian that represents the uncertainty of travel time prediction, t_{D_i} are the maxima of the detection function, and t_{g_i} the corresponding theoretical arrival times, the CMM function is maximised when $\sqrt{(\sigma_D^2 + \sigma_G^2)} = \Delta t_{rms}$ (Drew et al., 2013). For our downhole waveforms, the sampling rate is 0.5 ms, which is consistent with table 3-3. For the surface recordings, which were processed on a $12 \times 12 \times 12$ m grid ($40 \times 40 \times 40$ ft) and later interpolated to the $12 \times 12 \times 6$ m grid, the time window comprises 11 time samples: 5 samples before and 5 samples after the event detection time, with CMM cubes sampled every 2 ms. Again, the cube that contains the highest maximum likelihood value within the time window is used for location matching. Between all discrete time CMM cubes, the maximum likelihood locations rarely differ by more than 4 grid blocks or 48 m in horizontal direction between surface and downhole CMM cubes. An appropriate time window and sampling rate are important for obtaining good results. If the time window is too large, unrelated arrivals may contribute to the solution. If $\sigma_R^2 \ll \Delta t_{rms}$, the contributing signals are too sharp and the coalescence will be lost as Δt_w approaches Δt_{rms}.

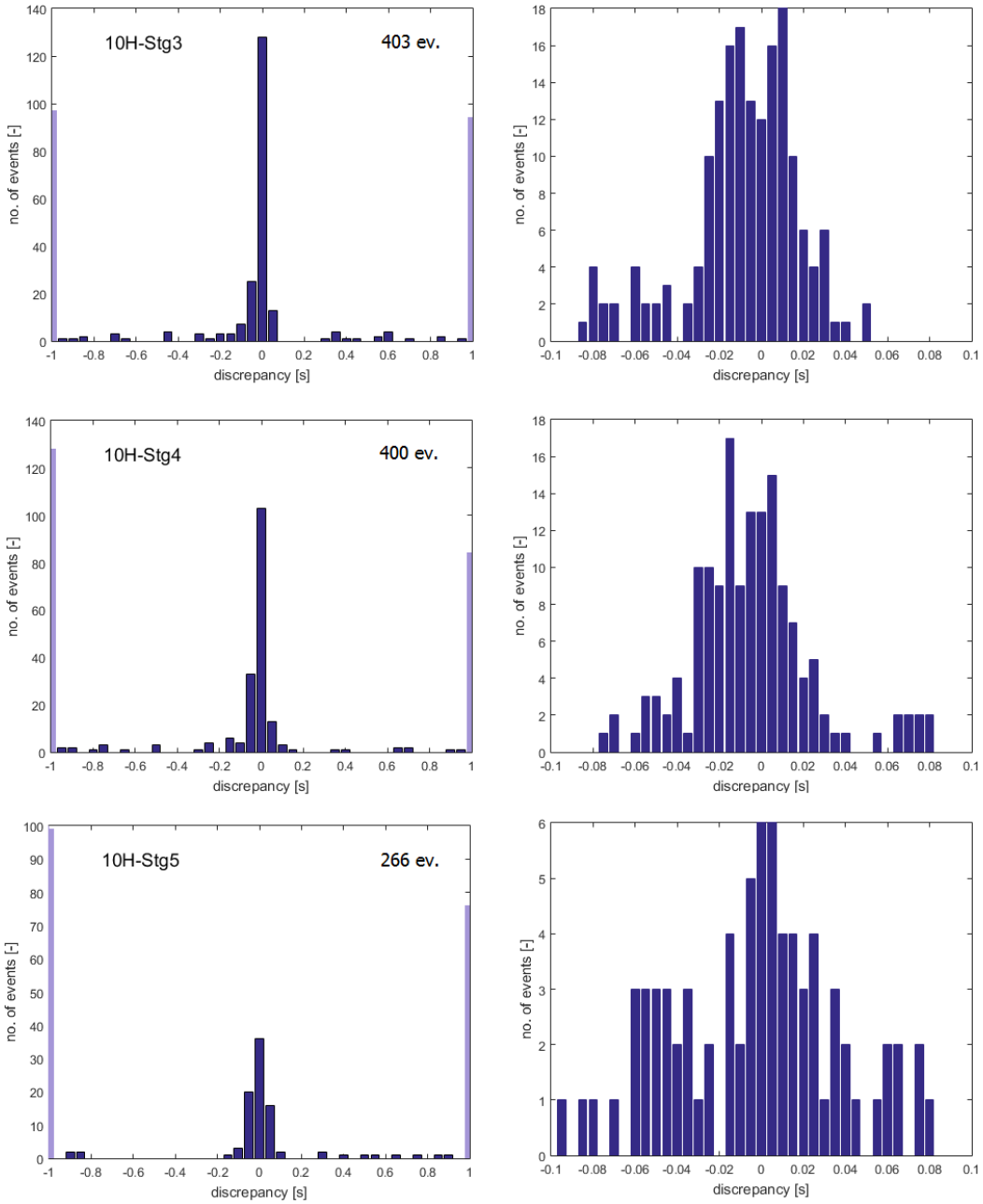

Figure 5-2: Quantification of time match discrepancies between downhole and surface events. Time differences are relative to the time of the closest arrival in the downhole dataset. Events detected within 0.070 seconds of one another were considered a match. The light purple bars on the side of the left-column plots denote the number of events with discrepancies outside the inverval (-1s, 1s).

5-2 Location Matching

Because surface detections are more certain in the horizontal plane than downhole detections, the X-Y slices of the downhole CMM cubes were multiplied with a Gaussian smoothing function with mean 0 and standard deviation σ:

$$f(x|0,\sigma) = \frac{1}{\sigma\sqrt{2\pi}} \quad e^{\frac{-x^2}{2\sigma^2}} \quad , \tag{5-2}$$

in order to relax the horizontal constraints imposed by the downhole CMM cube. The standard deviation of the smoothing function was carefully chosen to ensure balanced horizontal and vertical constraints, which results in a disc shaped CMM pdf that follows the slight dip of the reservoir. A lower standard deviation reduces the vertical location constraint, which could cause the product of both cubes to peak in a direction that is not necessarily always towards the horizontal X-Y location of the surface CMM cube. A higher standard deviation will relax the horizontal constraint given by the downhole array until the point that it simply assigns the depth of the event given by the downhole array at the horizontal point of intersection with the surface CMM cube with highest likelihood (figure 5-3).

Some CMM cubes match better than others. To constitute a good match, the X-Y locations of surface and downhole CMM cubes must exhibit less than 50 m separation. The surface CMM pdf should display an oval shape, with the long axis in an approximately vertical direction, and the downhole CMM pdf should have a disc shape that dips in the direction of the reservoir. Multiplication of such pdfs will result in a joint CMM shape that is compact in all directions (figure 5-4). An average match means that the downhole and surface event locations are 50-250 meters away from each other, and CMM shapes are similar to the CMM shapes that are considered 'good' (figure 5-5). A poor match is constituted by surface and downhole event locations that are separated more than 250 meters, or have anomalous CMM shapes whose multiplication results in relatively large joint CMM shapes (figure 5-6). If corresponding downhole and surface microseismic event locations displayed more than 300 m separation, they were not considered to be a match. Table 5-1 shows what percentage of joint locations were considered a good, average or poor location match, the histograms in figure 5-7 display the entire distribution of differences in maximum likelihood position estimates between surface and downhole CMM cubes.

Table 5-1: Good (0-50 m), average (>50 m - 250 m), poorly (>250 m - 300 m) and non-joint-located (>300 m) microseismic events per stage as a percentage of the total number of time-matched events.

	good	average	poor	non-located
10H3	59%	35%	3%	3%
10H4	12%	82%	1%	5%
10H5	14%	73%	6%	7%

Events that were not joint-located, are individually located around the fringes of both surface and downhole microseismic clouds, both in horizontal and in vertical direction (figure 5-8). Notice that there are outliers that are located farther than 300 m outside the core microseismic cloud, yet they are incorporated in the joint inversion, which proves that the method does not simply eliminate all outliers, but puts appropriate constraints on them.

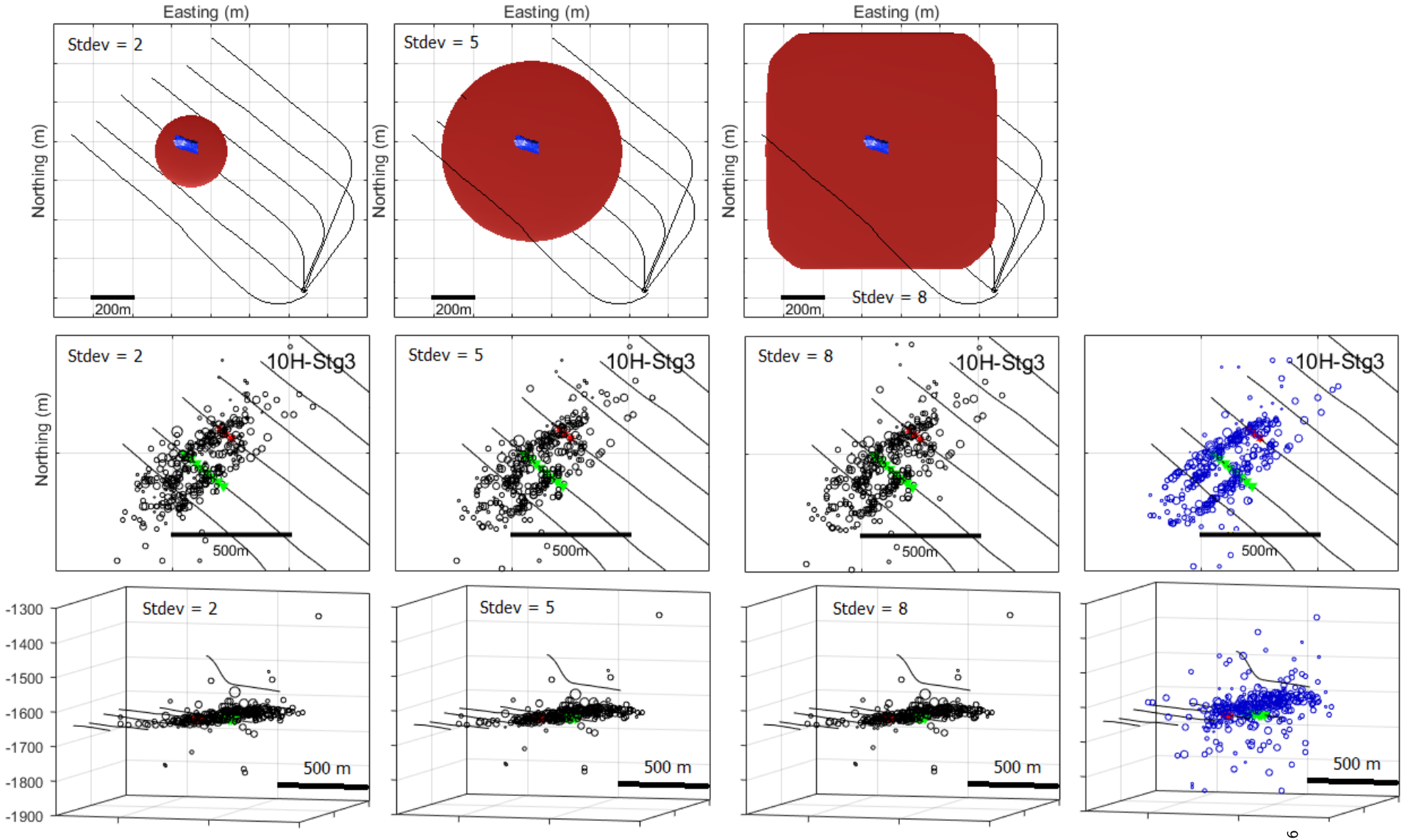

Figure 5-3: The effects of different smoothing functions on the joint inversion location for stage 10H3. Top row: downhole CMM shapes for different smoothing functions(red), surface (blue) for comparison. Second row: top view of joint microseismic event locations for different smoothing functions. Bottom row: Side view of joint microseismic event locations for different smoothing functions. 4th column: surface results for comparison. Note that the vertical constraint is good for all smoothing functions. Features of the joint microseismic cloud become more distinct by increasing the standard deviation from 2 to 5. Increasing further from 5 to 8 does not yield better features. Furthermore, the downhole CMM shape fills almost entirely the look-up-table. A standard deviation of 5 is used for the joint location. The isosurface value used to plot the CMM shapes is set at 75% of the maximum value.

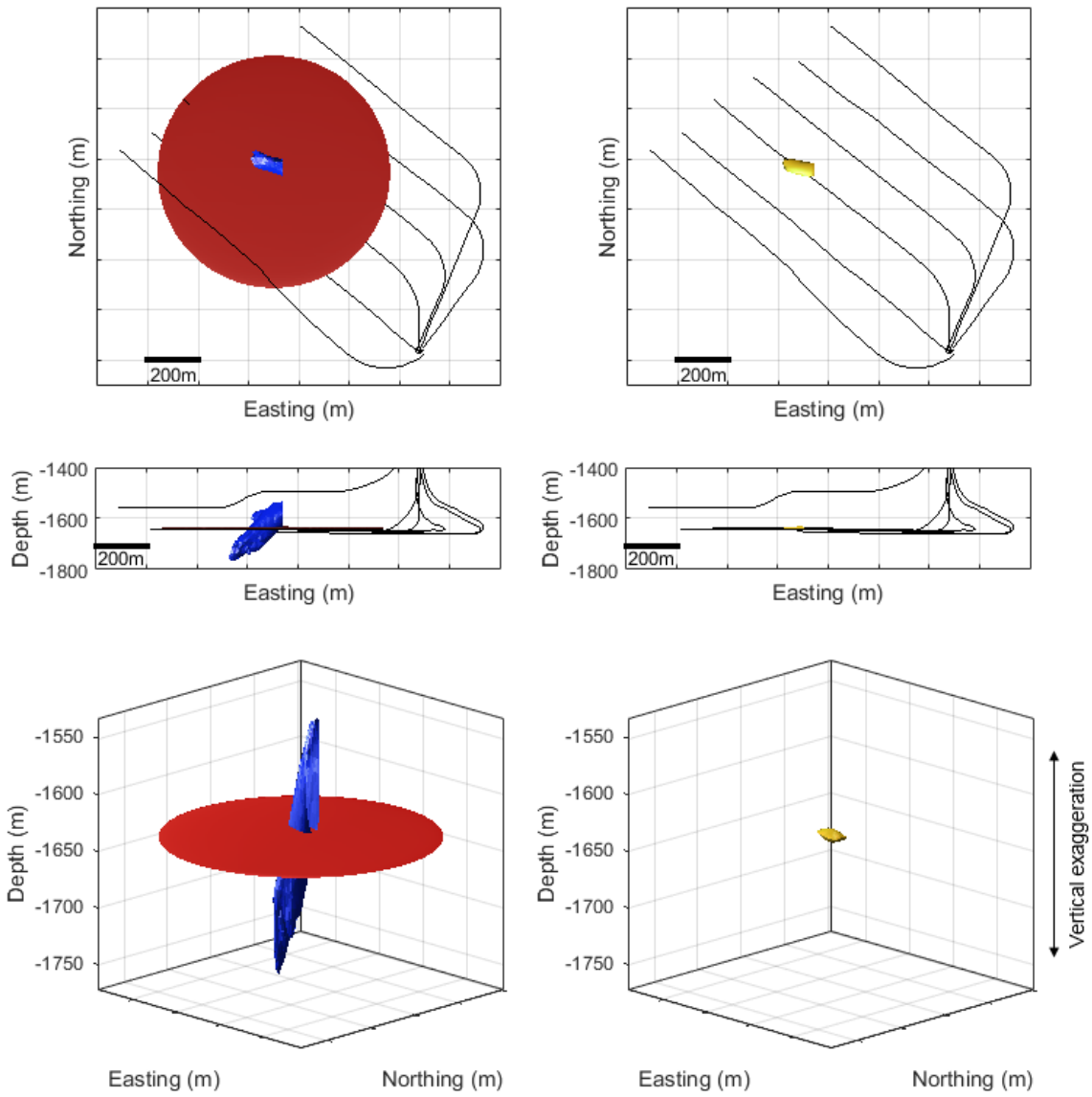

Figure 5-4: CMM shapes for an event that displays good spatial match. The isosurface value used to plot the CMM shapes is set at 75% of the maximum value. Blue is the surface CMM shape, red is the downhole CMM shape, yellow is the joint CMM shape. Upper plot displays a top view, the middle plot a side view from the south, the lower plot gives an overview of the shape in 3D. The centers of the surface and downhole CMM cubes are closely located, and their pdf shapes match the expected uncertainties.

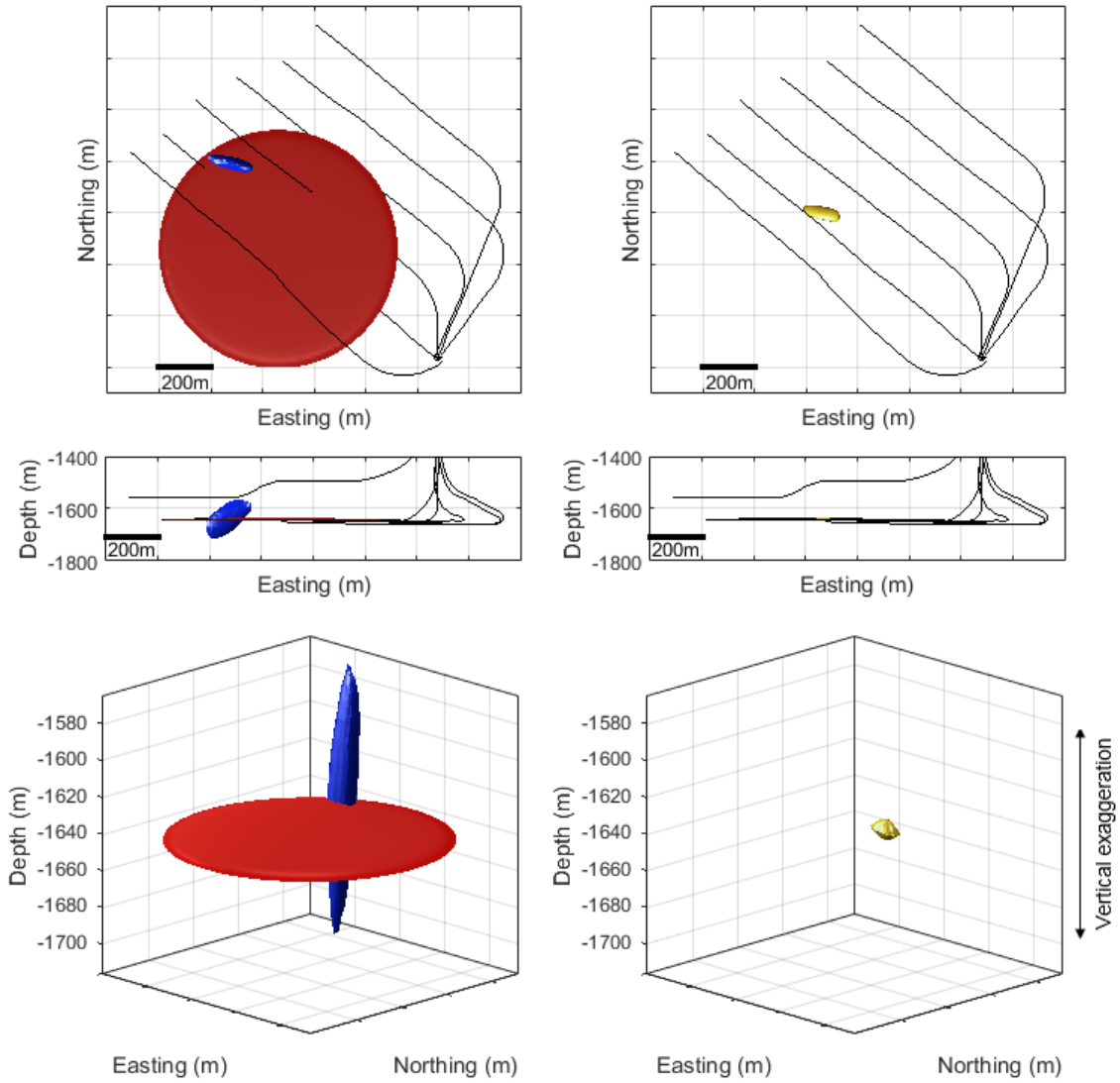

Figure 5-5: CMM shapes for an event that displays an average spatial match. The isosurface value used to plot the CMM shapes is set at 75% of the maximum value. Blue is the surface CMM shape, red is the downhole CMM shape, yellow is the joint CMM shape. Upper plot displays a top view, the middle plot a side view from the south, the lower plot gives an overview of the shape in 3D. The centers of the surface and downhole CMM cubes are within a 50 m - 250 m range, and their pdf shapes match the expected uncertainties.

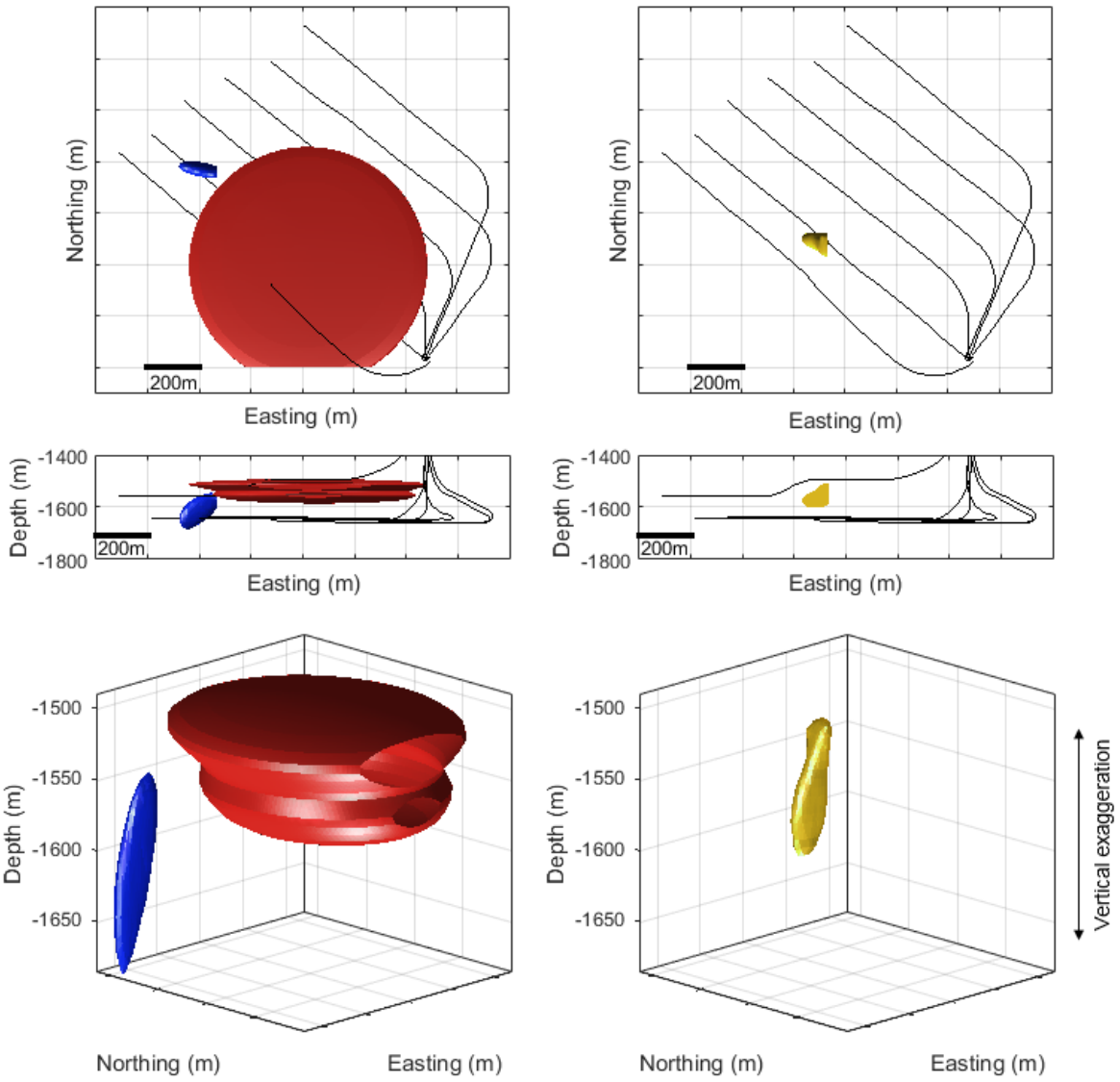

Figure 5-6: CMM shapes for an event that displays a poor spatial match. The isosurface value used to plot the CMM shapes is set at 75% of the maximum value. Blue is the surface CMM shape, red is the downhole CMM shape, yellow is the joint CMM shape. Upper plot displays a top view, the middle plot a side view from the south, the lower plot gives an overview of the shape in 3D. The downhole CMM shape seems to be a hybrid of two discs that is truncated on the edge of the look-up-table. The center of the surface CMM shape is relatively far away from the center of the downhole CMM shape, which culminates in a joint location that is somewhere in the middle of both centers, without much constraint on the vertical location of the event.

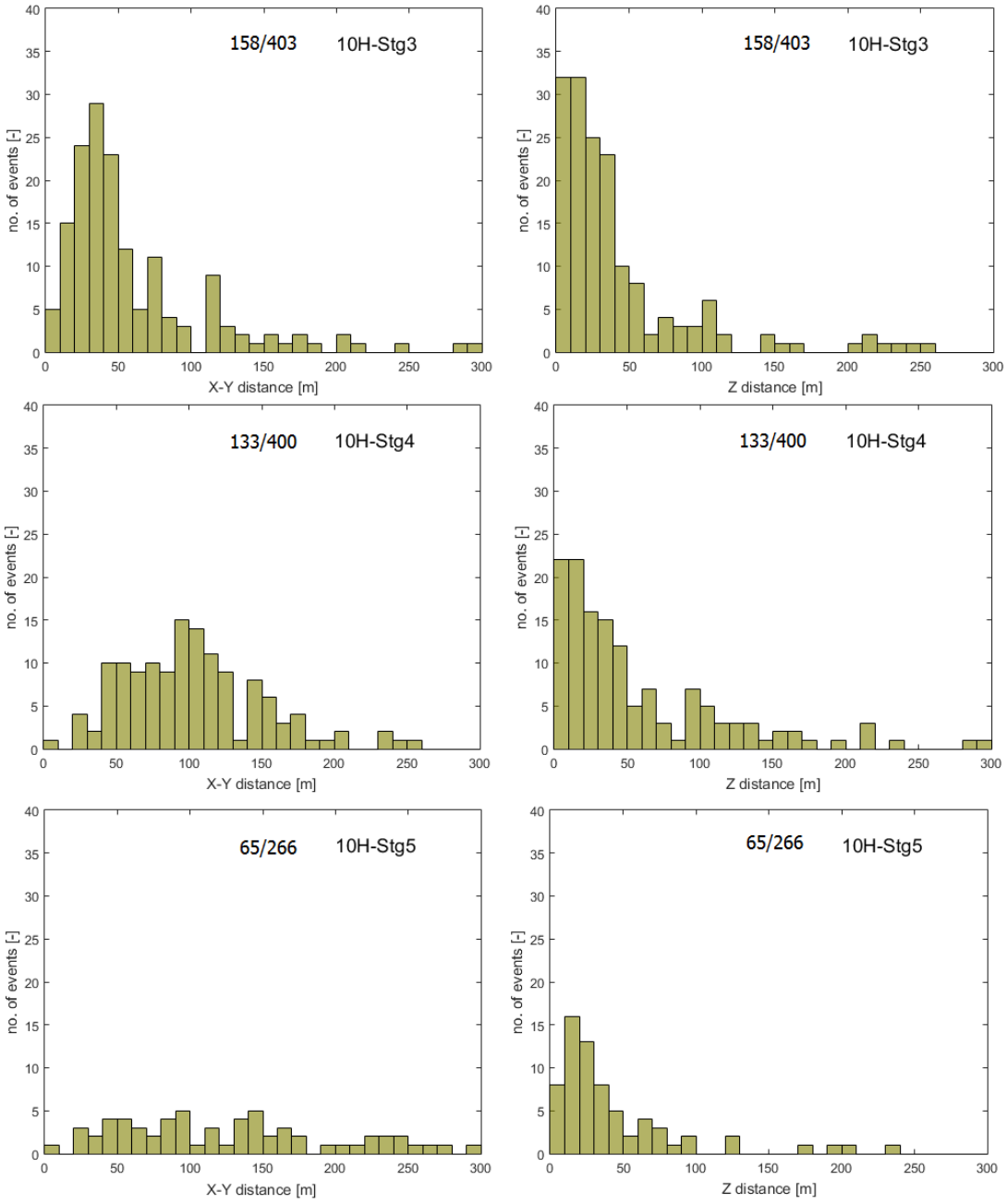

Figure 5-7: Distances between downhole and surface event locations. Left: location discrepancy in the horizontal direction. Right: vertical separation. Ratio at the top tells how many events were both time- and location matched out of all events in that stage.

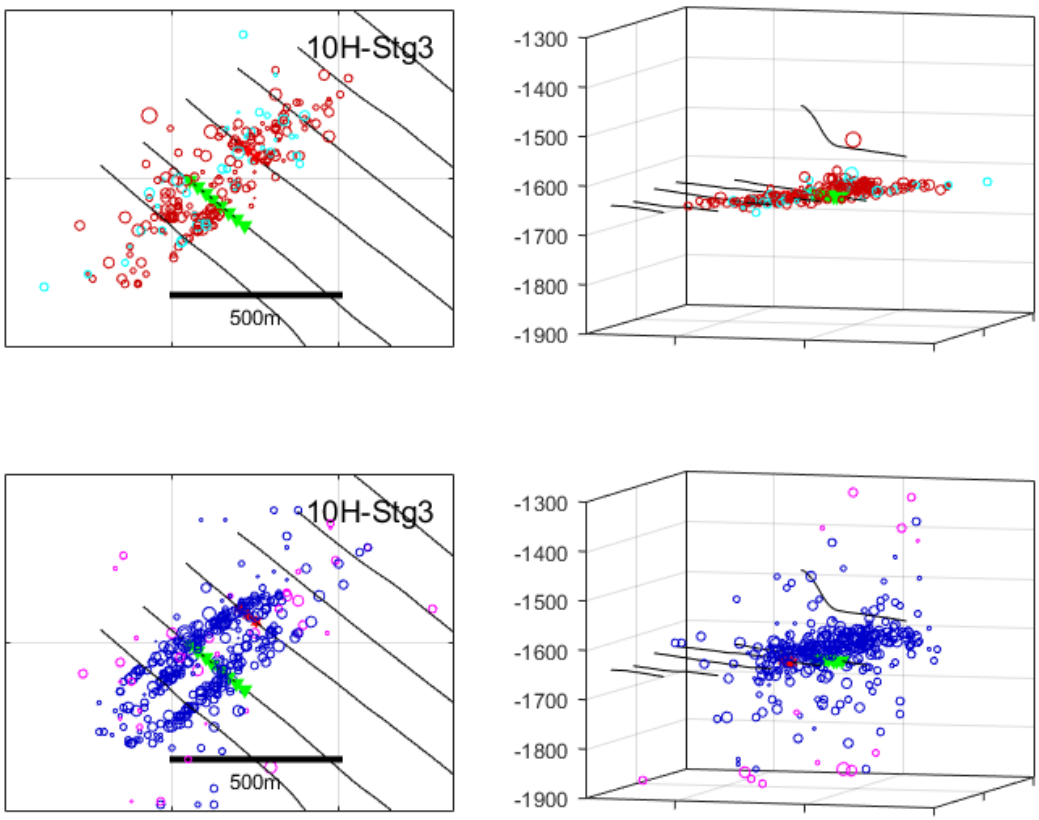

Figure 5-8: All microseismic events that were used in the joint-location attempt. Highlighted events did not contribute to the joint location because of a >300 m location mismatch between the surface and downhole CMM cube. Non-located events are concentrated on the fringes of the microseismic clouds, both vertically and horizontally. For downhole, microseismic events are denoted in red, with cyan for non-located events. For surface, microseismic events are denoted in blue, with magenta for non-located events.

5-3 Event Location from Joint CMM

The joint inversion was carried out for all stages under analysis. For stage 10H3 (figure 5-9), the same three distinct linear features that are also present in the surface cloud of microseismic events can be distinguished, yet the vertical direction the microseismic events are closer to the target layer, which is the effect that the downhole CMM cubes contribute. In stage 10H4 (figure 5-10), the same trend can be seen: the joint inversion shows significantly tighter localisation in the vertical direction compared to the surface microseismic cloud of events. Both surface and downhole show near identical features, but slightly shifted. This shift seems to have an adverse effect on the joint microseismic cloud, because it shows more dispersion than either downhole or surface, yet the main elongated feature is still very clear. Where there is little congruence between downhole and surface microseismic cloud structures, such as in 10H5 (figure 5-11), the joint inversion does an especially good job. The joint cloud for stage 10H5 is well constrained in depth and relies on the surface cloud for the X-Y locations. The combination looks more plausible than the microseismic clouds produced by surface or downhole monitoring alone.

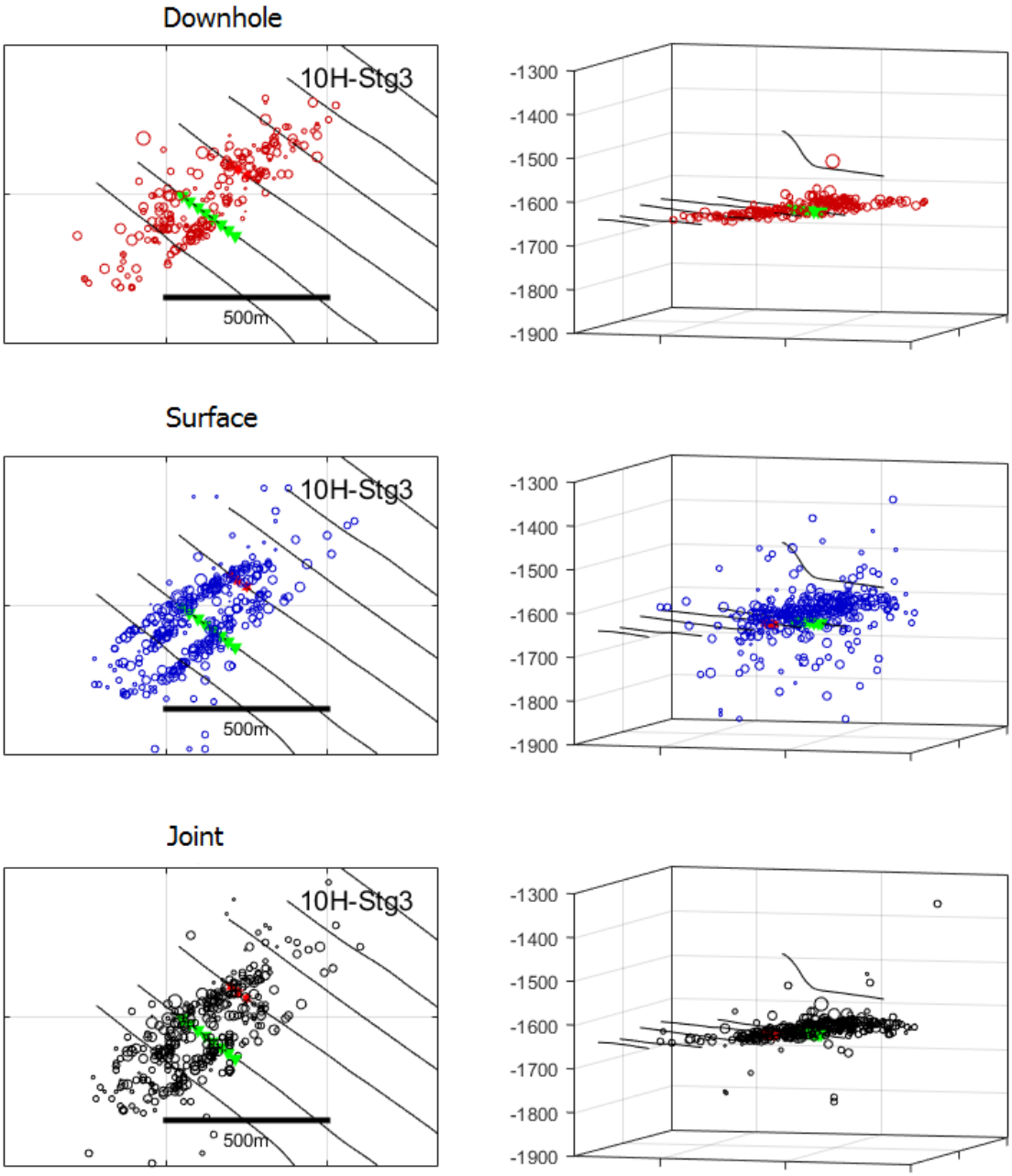

Figure 5-9: Joint solution for stage 10H3. Top: contributing downhole events (red), middle: contributing surface events (blue), bottom: joint event location. Left column: top view. Right column: side view. The joint location combines the strengths of surface and downhole microseismic clouds by adopting horizontal location information mostly from the surface microseismic cloud, and adopting depth location information mainly from the downhole microseismic cloud.

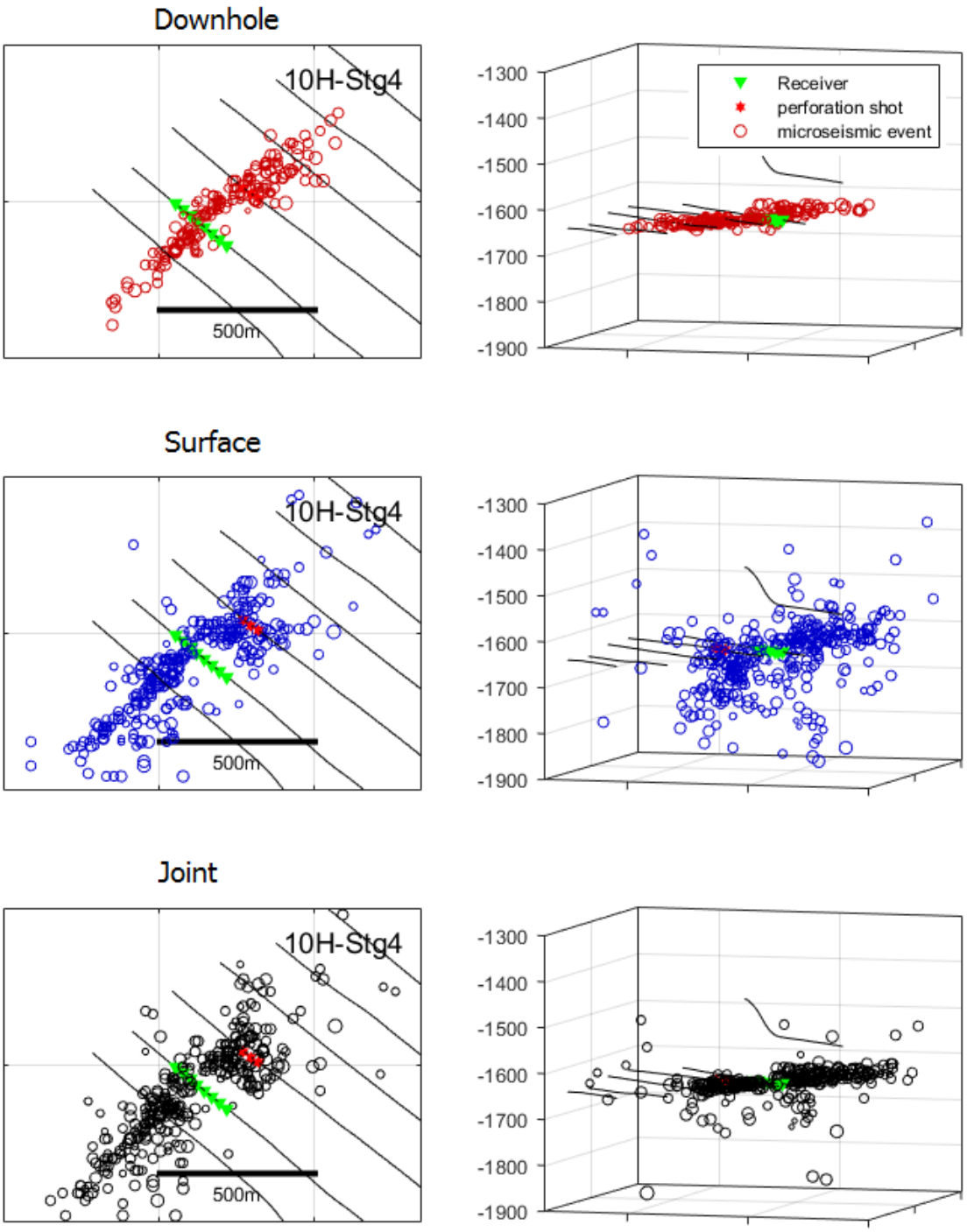

Figure 5-10: Joint solution for stage 10H4. Top: contributing downhole events (red), middle: contributing surface events (blue), bottom: joint event location. Left column: top view. Right column: side view. The joint location combines the strengths of surface and downhole microseismic clouds by adopting horizontal location information mostly from the surface microseismic cloud, and adopting depth location information mainly from the downhole microseismic cloud. Yet the horizontal structure looks more scattered than either the surface or downhole microseismic cloud.

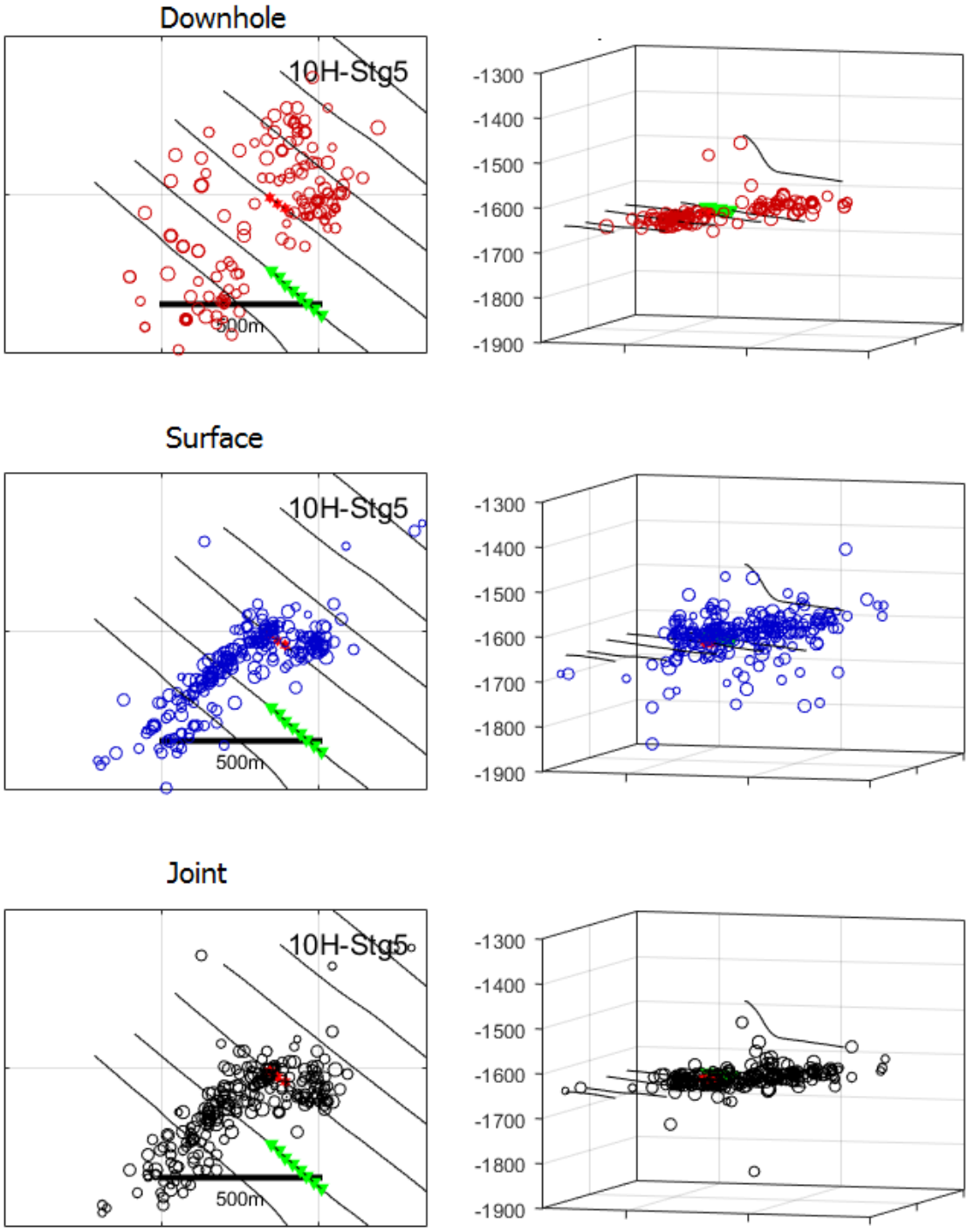

Figure 5-11: Joint solution for stage 10H5. Top: contributing downhole events (red), middle: contributing surface events (blue), bottom: joint event location. Left column: top view. Right column: side view. The joint location combines the strengths of surface and downhole microseismic clouds by adopting horizontal location information mostly from the surface microseismic cloud, and adopting depth location information mainly from the downhole microseismic cloud.

Chapter 6

Conclusion and Discussion

Passive seismic monitoring is done during hydraulic fracturing operations to locate induced fractures, estimate the stimulated volume, and allow intervention when undesired areas are being stimulated. In this study, a hydraulic stimulation operation was monitored simultaneously by means of a downhole receiver array, near the area of stimulation, and by a large receiver geometry at the surface, laid out in a radial fashion above the stimulated area. The data from each technique were first processed separately, both by means of coalescence microseismic mapping, which yields, besides a location estimate, a four-dimensional probability distribution function that describes the spatio-temporal uncertainty associated with each microseismic event. Subsequently, the collection of pdfs of both monitoring techniques are combined to form a joint location estimate.

6-1 Downhole Monitoring

P-, Sh- and Sv-waves were used to determine the location of perforation shots and microseismic events. Furthermore, the effects of an HTI (horizontal transversely isotropic) velocity model on microseismic event location was investigated and compared to location results obtained from a VTI (vertical transversely isotropic) velocity model. Due to fixing the Vp/Vs ratio, but not the absolute velocity during source parameter estimation, the HTI model was allowed to exhibit higher velocities than the VTI model, which translated into slightly higher magnitudes of inverted microseismic events for the HTI model than for the VTI model. A denser cloud of events near the downhole monitoring array was also retrieved with the HTI model, which is the result of better modeling of wave arrival times at angles away from the normal to the tool array. A number of seismic attributes (orthogonality, confidence factor, uncertainty ellipsoid and magnitude) were used to filter out unreliable events, which, on average, brought $\sim$2000 triggers over a 2.5 hour timespan back to $\sim$400 good quality event locations. The VTI model exhibits a relationship between traveltime residuals and the angle of incidence, which causes events with a larger angle of incidence to have a larger location uncertainty. The HTI velocity model was able to resolve the incidence-angle dependent uncertainty bias. HTI locates the

microseismic events consistently closer to the receiver than the VTI velocity model, which may be attributed to the difference in velocity between HTI and VTI. Furthermore, features in the microseismic clouds that may be interpreted as representing fracture planes are apparently more linear from the HTI model than from the VTI model. Assuming a straight fracture geometry, the HTI model potentially provides a better horizontal location, however, we do not know the exact fracture geometry and the curvature observation is within the margin of interpretation. When looking at the vertical constraint the borehole monitoring provides, the VTI model consistently locates events within the target layer, whereas the HTI model displays a larger vertical spread. Since the well geometry is the same for both models, the tighter depth localisation of the VTI model must be due to the fact that it is layered, in contrast to the homogeneous HTI model (see figure 3-2). The VTI model is derived from well-logs in the vertical section of the borehole and so is likely to capture layering effects more realistically than the HTI model. Since there are large velocity contrasts at the boundaries of the target layer, the VTI LUT travel times will change rapidly for locations outside the target layer, and is likely to result in poor focusing of the Gaussian-modelled pdf functions in CMM. By contrast, the uniform HTI velocity function will have no sharp changes in LUT with depth and so there will be a greater chance of finding acceptable focusing of the pdf functions at locations outside the target layer. From the comparison between HTI and VTI it is suggested that the HTI model, when implemented in a layered velocity model that is derived from well logs, will provide more accurate location estimates than the VTI model. Since Becker (2015) found that vertical anisotropy cannot be neglected, subsequent microseismic event analysts are advised to consider orthorhombic anisotropic velocity models for fractured shales.

6-2 Surface Monitoring

Due to attenuation of wave energy in the overburden, surface processing only made use of P-wave arrivals. Since surface monitoring is less sensitive than downhole monitoring, events detected by the surface array must be relatively large, and therefore relatively reliable events. For this reason, and for the lack of seismic attributes, no filtering was performed on the surface-detected microseismic events. The large aperture of the surface array made it possible to constrain the horizontal location of the microseismic events well, and clear structures in the microseismic cloud supported the decision not to filter the surface-detected events. In the vertical direction, microseismic event location by surface monitoring proves less accurate because S-wave information cannot be used and long offset receiver positions do not receive enough energy to constrain event location. Even though the vertical position is not well constrained, surface monitoring does detect the slight dip in the reservoir.

6-3 Joint Inversion

To obtain the joint solution, for each stage, roughly 400 downhole event detections were attempted to be matched in time to roughly 400 surface detections, with success rates of up to 40 percent. Events that coincided within a 70 ms window were considered a match. When considering that downhole monitoring yielded on average >2000 detections, which were filtered down to ∼400 events before time matching, it can be said that both filtering

and time-match were successful. Subsequently, the time-matched events were matched in space, by requiring corresponding surface and downhole microseismic events to be within 300 m proximity of one another. This was done with a success rate of ∼95 percent. Next, the downhole CMM cubes were multiplied by a Gaussian smoothing function that relaxed the downhole horizontal constraint, in order to harvest the horizontal constraint from the surface event detections. Multiplication of the surface CMM cubes with the smoothed downhole CMM cubes resulted in the joint solution. The joint surface-downhole located microseismic clouds show a horizontal structure that is similar to the structure obtained from surface monitoring, and nearly all events are located within the target layer.

6-4 Future Research

Future research in joint-surface downhole monitoring should be focussed on exploring different techniques for combining surface and downhole CMM cubes into a joint location. The joint inversion methodology followed here multiplies the surface and downhole CMM cubes that contain the maximum likelihood origin time estimates. Because of project time constraints, only this joint inversion methodology was tried. Other interesting approaches could include an exhaustive multiplication of each surface CMM cube within a specified time window around the detection time with each downhole CMM cube within a specified time window around the detection time. The joint solution would be the multiplied CMM cube that exhibits the highest maximum likelihood location or the one with the lowest standard deviation after multiplication. Alternatively, one could sum all discrete time CMM cubes within the time window and then normalise the summed cube to form an 'average' CMM cube for both the downhole and surface event, and subsequently multiply these two 'average' cubes to form a joint CMM cube. Yet another approach could be to cross correlate or convolve all discrete time cubes for each method, and multiply, cross correlate or convolve the two resulting cubes. From examining discrete time CMM cubes, we know that maximum likelihood location estimates within a 10 ms window rarely vary more than 50 meters, and usually much less. Therefore, the effect of these alternative methods on a complete microseismic cloud may be hard to evaluate.

Since theoretically, the microseismic events occuring close to the downhole receivers, are more reliable than microseismic events occurring far away from the downhole receiver, it would be interesting to see the effects of a weighted multiplication that increases the importance of downhole event location close to the downhole array, and that discounts downhole locations of events far away from the array. However, this can only be done by virtue of the closest events being indeed more certain than far away events, which, for the current VTI model, is not the case.

Bibliography

Aki, K. and Richards, P. G. (1980). *Quantitative Seismology*, volume 1. University Science Books.

Anderson, E. (1905). The dynamics of faulting. *Transactions of the Edinburgh Geological Society*, 8(3):387–402.

Anikiev, D., Valenta, J., Staněk, F., and Eisner, L. (2014). Joint location and source mechanism inversion of microseismic events: benchmarking on seismicity induced by hydraulic fracturing. *Geophysical Journal International*, 198(1):249–258.

Backus, G. E. (1962). Long-wave elastic anisotropy produced by horizontal layering. *Journal of Geophysical Research*, 67(11):4427–4440.

Bardainne, T. and Gaucher, E. (2010). Constrained tomography of realistic velocity models in microseismic monitoring using calibration shots. *Geophysical prospecting*, 58(5):739–753.

Baysal, E., Kosloff, D. D., and Sherwood, J. W. (1983). Reverse time migration. *Geophysics*, 48(11):1514–1524.

Becker, T. (2015). Moment tensor inversion using combined surface and downhole hydraulice fracture monitoring. Master's thesis, Eidgenössische Technische Hochschule Zürich, Zurich, Switzerland.

Bender, B. (1983). Maximum likelihood estimation of b values for magnitude grouped data. *Bulletin of the Seismological Society of America*, 73(3):831–851.

Blias, E. and Grechka, V. (2013). Analytic solutions to the joint estimation of microseismic event locations and effective velocity model. *Geophysics*, 78(3):KS51–KS61.

BP (2016). Bp energy outlook 2016 edition: Outlook to 2035. British Petroleum website, bp.com/energyoutlook.

Bradford, I., Probert, T., Raymer, D., Ozbek, A., Primiero, P., Kragh, E., Drew, J., and Woerpel, C. (2013). Application of coalescence microseismic mapping to hydraulic fracture monitoring conducted using a surface array. In *75th EAGE Conference & Exhibition incorporating SPE EUROPEC 2013*.

Brune, J. N. (1970). Tectonic stress and the spectra of seismic shear waves from earthquakes. *Journal of geophysical research*, 75(26):4997–5009.

Ciezobka, J. (2012). Marcellus shale gas project 0912204. topical report 2. Research Partnership for America website, www.rpsea.org.

Coleman Jr, J. L., Milici, R. C., Cook, T. A., Charpentier, R. R., Kirshbaum, M., Klett, T. R., Pollastro, R. M., and Schenk, C. J. (2011). Assessment of undiscovered oil and gas resources of the devonian marcellus shale of the appalachian basin province. Technical report, US Geological Survey.

De La Pena, A., Wessels, S., Gunnell, A., Numa, K., Williams-Stroud, S., Eisner, L., Thornton, M., and Mueller, M. (2011). Fault or frac? source mechanism and b-value detection of fault fracturing-a barnett case study. In *73rd EAGE Conference and Exhibition incorporating SPE EUROPEC 2011*.

Drew, J., White, R. S., Tilmann, F., and Tarasewicz, J. (2013). Coalescence microseismic mapping. *Geophysical Journal International*, 195(3):1773–1785.

Duncan, P. and Eisner, L. (2010a). Reservoir characterization using surface microseismic monitoring: Geophysics 75. *75A139–75A146, doi*, 10(1.3467760).

Duncan, P. M. and Eisner, L. (2010b). Reservoir characterization using surface microseismic monitoring. *Geophysics*, 75(5):139–146.

Economides, M. J., Nolte, K. G., Ahmed, U., and Schlumberger, D. (2000). *Reservoir stimulation*, volume 18. Wiley Chichester.

Eisner, L., Duncan, P. M., Heigl, W. M., and Keller, W. R. (2009). Uncertainties in passive seismic monitoring. *The Leading Edge*, 28(6):648–655.

Eisner, L., Gei, D., Hallo, M., Opršal, I., and Ali, M. Y. (2013). The peak frequency of direct waves for microseismic events. *Geophysics*, 78(6):A45–A49.

Eisner, L., Gei, D., Hallo, M., Oprsal, I., and Ali, M. Y. (2014). Source reverberations, near-surface resonances, or q? comment on" the peak frequency of direct waves for microseismic events"(leo eisner, davide gei, miroslav hallo, ivo oprsal, and mohammed y. ali, geophysics, 78, no. 6, a45-a49) reply.

Evans, K. F., Cornet, F. H., Hashida, T., Hayashi, K., Ito, T., Matsuki, K., and Wallroth, T. (1999). Stress and rock mechanics issues of relevance to hdr/hwr engineered geothermal systems: review of developments during the past 15 years. *Geothermics*, 28(4):455–474.

Geiger, L. (1910). Herdbestimmung bei erdbeben aus den ankunftszeiten. *Nachrichten von der Gesellschaft der Wissenschaften zu Göttingen, Mathematisch-Physikalische Klasse*, 1910:331–349.

Gendrin, A., Özbek, A., Probert, T., Bradford, I., and Le Calvez, J. (2016). Toward an optimized data conditioning for surface-acquired microseismic data. In *78th EAGE Conference & Exhibition Vienna*.

Grechka, V. (2015). Tilted ti models in surface microseismic monitoring. *Geophysics*, 80(6):WC11–WC23.

Grechka, V., De La Pena, A., Schisselé-Rebel, E., Auger, E., and Roux, P.-F. (2015). Relative location of microseismicity. *Geophysics*, 80(6):WC1–WC9.

Grechka, V. and Yaskevich, S. (2013). Azimuthal anisotropy in microseismic monitoring: A bakken case study. *Geophysics*, 79(1):KS1–KS12.

Gutenberg, B. and Richter, C. F. (1956). Magnitude and energy of earthquakes. *Annals of Geophysics*, 9(1):1–15.

Hubbert, M. K. and Willis, D. G. (1957). Mechanics of hydraulic fracturing. *AIME petroleum transactions*, 210:153–163.

Kanamori, H. (1977). The energy release in great earthquakes. *Journal of geophysical research*, 82(20):2981–2987.

Kanasewich, E., Hemmings, C., and Alpaslan, T. (1973). Nth-root stack nonlinear multichannel filter. *Geophysics*, 38(2):327–338.

Kolinsky, P., Eisner, L., Grechka, V., Jurick, D., and Duncan, P. (2009). Observation of shear-wave splitting from microseismicity induced by hydraulic fracturing–a non-vti story. In *71st EAGE Conference and Exhibition incorporating SPE EUROPEC 2009*.

Li, J., Li, C., Morton, S. A., Dohmen, T., Katahara, K., and Nafi Toksöz, M. (2014). Microseismic joint location and anisotropic velocity inversion for hydraulic fracturing in a tight bakken reservoir. *Geophysics*, 79(5):C111–C122.

Maxwell, S., Rutledge, J., Jones, R., and Fehler, M. (2010). Petroleum reservoir characterization using downhole microseismic monitoring. *Geophysics*, 75(5):75A129–75A137.

Maxwell, S. C. (2011). What does microseismic tell us about hydraulic fracture deformation. *CSEG Recorder*, 36(8):31–45.

Meagher, D. J. (1980). *Octree encoding: A new technique for the representation, manipulation and display of arbitrary 3-d objects by computer*. Electrical and Systems Engineering Department Rensseiaer Polytechnic Institute Image Processing Laboratory.

Miller, H. G. and Singh, V. (1994). Potential field tilta new concept for location of potential field sources. *Journal of Applied Geophysics*, 32(2-3):213–217.

Mizuno, T., Leaney, S., and Michaud, G. (2010). Anisotropic velocity model inversion for imaging the microseismic cloud. In *72nd EAGE Conference and Exhibition incorporating SPE EUROPEC 2010*.

Morozov, I. B., Eisner, L., Gei, D., Hallo, M., Opršal, I., and Ali, M. Y. (2014). Reply to the discussion. *Geophysics*, 79(4):X19–X22.

Mueller, M., Thornton, M., and Eisner, L. (2011). Uncertainty in surface microseismic monitoring. *ASEG Extended Abstracts*, 2013(1):1–4.

Neuhaus, C. W., Williams-Stroud, S. C., Remington, C., Barker, W., Blair, K., Neshyba, G., McCay, T., et al. (2012). Integrated microseismic monitoring for field optimization in the marcellus shale-a case study. In *SPE Canadian Unconventional Resources Conference*. Society of Petroleum Engineers.

Özbek, A., Probert, T., Raymer, D., and Drew, J. (2013). Nonlinear processing methods for detection and location of microseismic events. In *75th EAGE Conference & Exhibition incorporating SPE EUROPEC 2013*.

Pearson, C. (1981). The relationship between microseismicity and high pore pressures during hydraulic stimulation experiments in low permeability granitic rocks. *Journal of Geophysical Research: Solid Earth*, 86(B9):7855–7864.

Peyret, O., Drew, J., Mack, M., Brook, K., Maxwell, S. C., Cipolla, C. L., et al. (2012). Subsurface to surface microseismic monitoring for hydraulic fracturing. In *SPE Annual Technical Conference and Exhibition*. Society of Petroleum Engineers.

Probert, T., Raymer, D., and Bradford, I. (2013). Comparing near-surface and deep-well microseismic data and methods for hydraulic fracture monitoring. In *4th EAGE Passive Seismic Workshop*.

PwC, F. (2013). Shale oil: The next energy revolution.

Rutledge, J., Phillips, W., and Mayerhofer, M. (2004). Faulting induced by forced fluid injection and fluid flow forced by faulting: An interpretation of hydraulic-fracture microseismicity, carthage cotton valley gas field, texas. *Bulletin of the Seismological Society of America*, 94(5):1817–1830.

Rutledge, J. T. and Phillips, W. S. (2003). Hydraulic stimulation of natural fractures as revealed by induced microearthquakes, carthage cotton valley gas field, east texas. *Geophysics*, 68(2):441–452.

Sayers, C. M. (2005). Seismic anisotropy of shales-what determines the sign of thomsen's delta parameter? In *67th EAGE Conference & Exhibition*.

Schimmel, M. and Paulssen, H. (1997). Noise reduction and detection of weak, coherent signals through phase-weighted stacks. *Geophysical Journal International*, 130(2):497–505.

Scholz, C. H. (2002). *The mechanics of earthquakes and faulting*. Cambridge university press.

Thomsen, L. (1986). Weak elastic anisotropy. *Geophysics*, 51(10):1954–1966.

U.S. Energy Information Administration (April 2016). Drilling productivity report for key tight oil and shale gas regions. Energy Information Administration website, http://www.eia.gov/petroleum/drilling/pdf/dpr-full.pdf.

Van Renterghem, C., Probert, T., Bradford, I., Özbek, A., and Robertsson, J. (2015). Factors influencing the surface expressions of perforation shots. In *77th EAGE Conference and Exhibition 2015*.

Warpinski, N. (2009). Integrating microseismic monitoring with well completions, reservoir behavior, and rock mechanics. *SPE 125239 presented at the SPE Tight Gas Completions Conference, San Antonio, Texas, USA, 15-17 June*.

Warpinski, N., Wolhart, S., and Wright, C. (2004). Analysis and prediction of microseismicity induced by hydraulic fracturing. spej 9 (1): 24–33. Technical report, SPE-87673-PA. DOI: 10.2118/87673-PA.

Whitmore, N. et al. (1983). Iterative depth migration by backward time propagation. In *1983 SEG Annual Meeting*. Society of Exploration Geophysicists.

Williams, M. J. and Calvez, J. L. (2013). Reconstructing frequency-magnitude statistics from detection limited microseismic data. *Geophysical Prospecting*, 61(s1):20–38.

Wong, J., Han, L., Bancroft, J., and Stewart, R. (2009). Automatic time-picking of first arrivals on noisy microseismic data. *CSEG. 0 0.2 0.4 0.6 0.8*, 1(1.2):1–4.

Zhang, H. and Thurber, C. (2003). Double-difference tomography: method and application to the hayward fault, california. *Bulletin of the Seismological Society of America*, 93(5):1875–1899.

Appendix A

A-1 Joint inversion time match

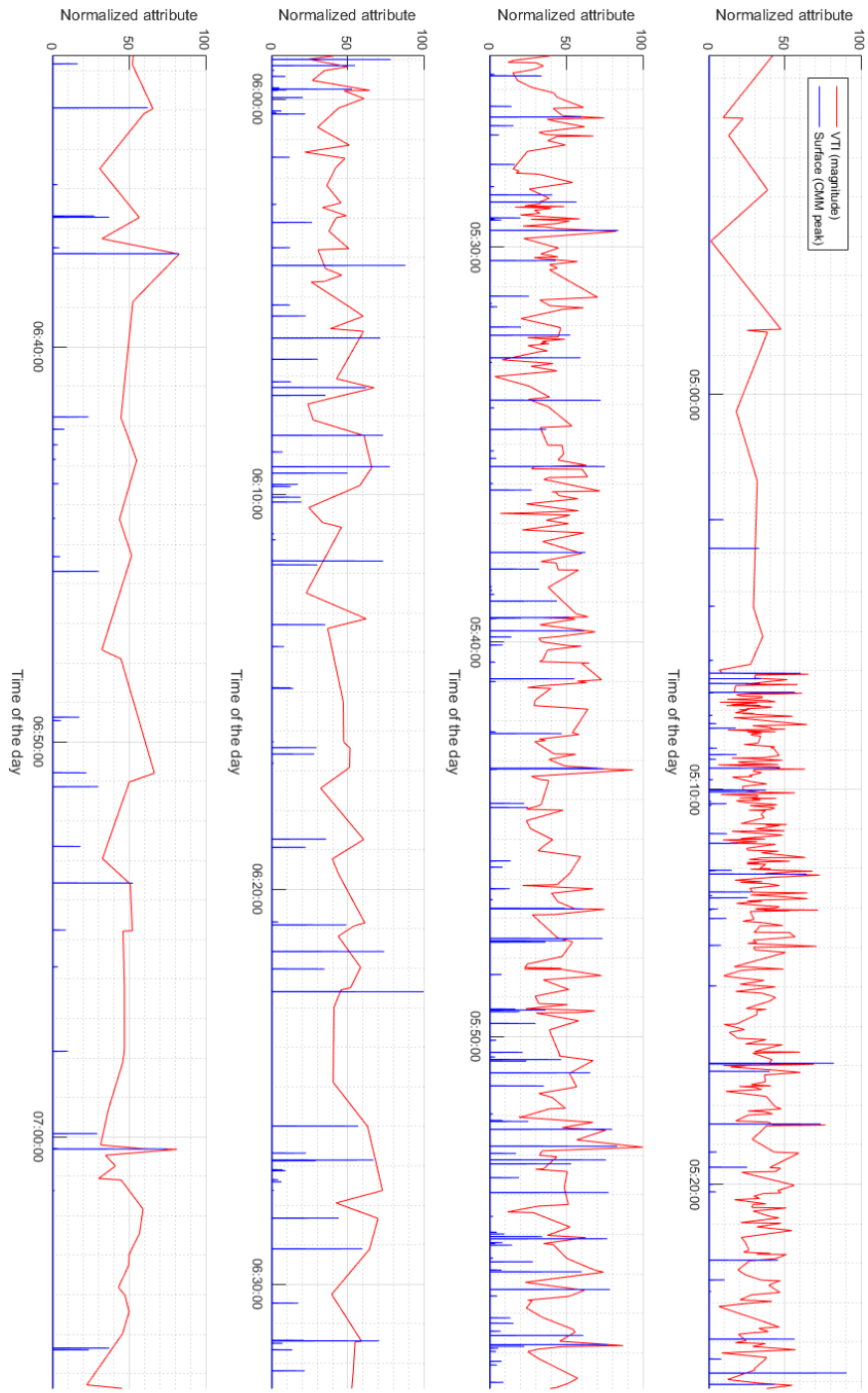

Figure A-1: Results of a time match between VTI downhole and surface microseismic recordings for stage 10H4. Blue spikes represent surface array detections, kinks in the red line denote downhole array detections.

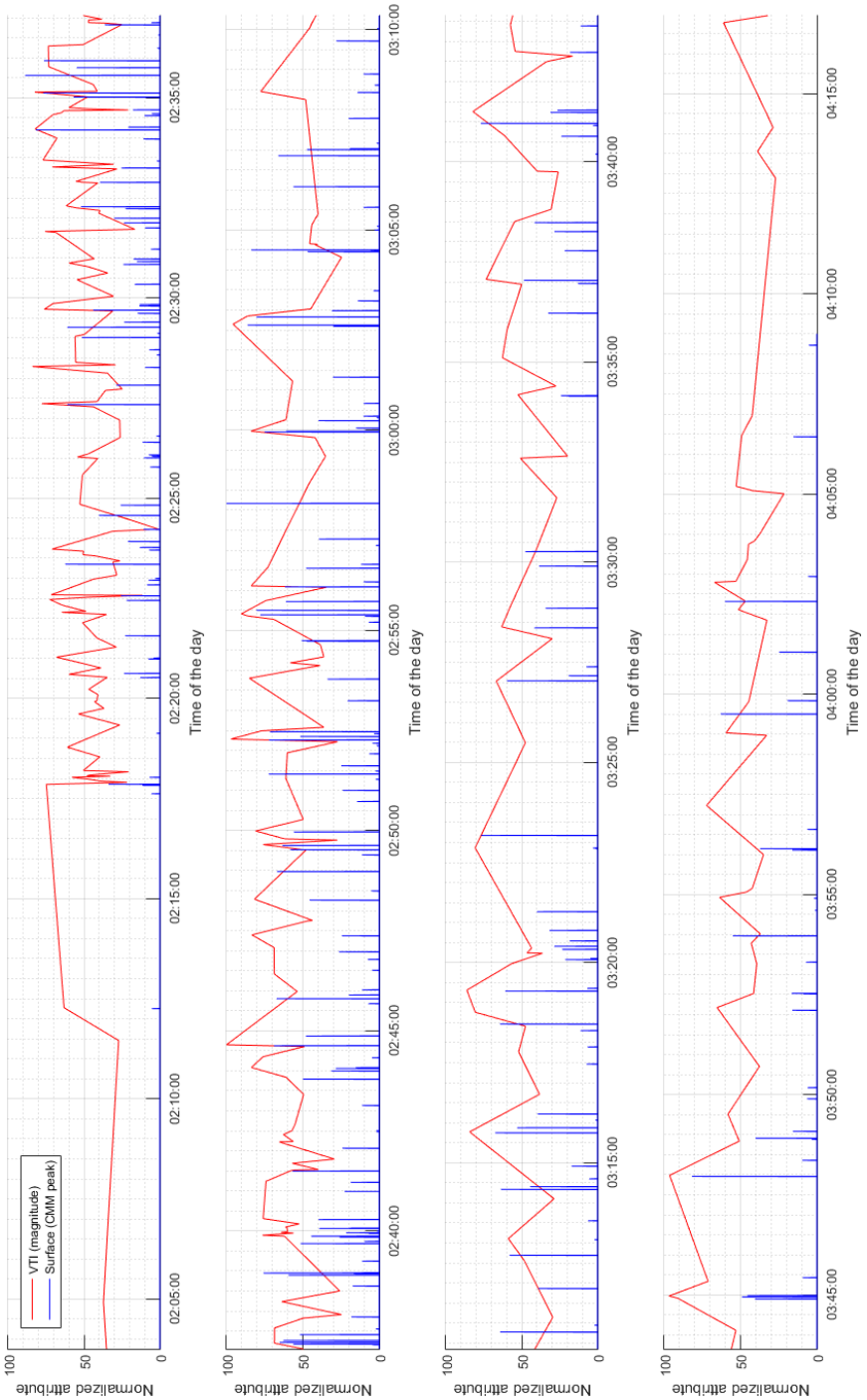

Figure A-2: Results of a time match between VTI downhole and surface microseismic recordings for stage 10H5. Blue spikes represent surface array detections, kinks in the red line denote downhole array detections.